DEPOSITIONAL BEHAVIORS OF TRACE METALS AROUND HYDROTHERMAL VENTS IN THE SCOTIA SEA

By

CALLI M. PROVENZA

Bachelor of Science in Geology

Texas A&M University

College Station, TX

2019

Submitted to the Faculty of the
Graduate College of the
Oklahoma State University
in partial fulfillment of
the requirements for
the Degree of
MASTER OF SCIENCE
December, 2022

DEPOSITIONAL BEHAVIORS OF TRACE METALS

AROUND HYDROTHERMAL VENTS IN THE

SCOTIA SEA

Thesis Approved:

Dr. Natascha Riedinger

Thesis Advisor

Dr. Ashley Burkett

Dr. Tracy Quan

ACKNOWLEDGEMENTS

I would like to thank the faculty of the Boone Pickens School of Geology for affording me opportunity to conduct research and further my education at Oklahoma State University. I have enjoyed learning more about my focus in geochemistry, as well as learning other aspects of geology such as basin analysis with Dr. Pashin and remote sensing with Dr. Mohamed. Additionally, I would like to thank my research advisor, Dr. Natascha Riedinger for advising and mentoring me throughout my time conducting research for my thesis project. I have learned a great deal from her and will use my newfound knowledge for the remainder of my career in geoscience. I would also like to thank her for allowing me to use her laboratory to work on samples she obtained from the R/V Polarstern expedition PS-119. I would also like to thank my committee members, Dr. Quan and Dr. Burkett for their continued support and mentorship in writing my thesis and using their laboratory facilities to conduct aspects of my research. I could not have completed this program without any of them. Next, I would like to thank my lab mates, Lauren Haygood and Alison Veresh, as well as the extended member Chris Jones who is current studying at University of California Davis-Riverside for their support, friendship, and helping run my samples for this study.

Without the financial assistance from many people within the Geological Society of America (GSA) and the Howard Lipman Foundation, as well as the Martin Family, this study would not have been possible. Therefore, I would like to deeply thank them for financially supporting me throughout my time at Oklahoma State University. I would also like thank the generous donors affiliated with the Walker Geology Scholarship and Devon Energy for their financial support as well. Without their generosity, I would not have been able to complete this study.

Lastly, I would like to thank my family and friends for their encouragements and motivation to see this master's project to the end.

Name: CALLI M. PROVENZA

Date of Degree: DECEMBER, 2022

Title of Study: DEPOSITIONAL BEHAVIORS OF TRACE METALS AROUND HYDROTHERMAL VENTS IN THE SCOTIA SEA

Major Field: GEOLOGY

Abstract: Sediment deposition along the East Scotia Ridge (ESR) in the Southern Ocean is dominated by biogenic sediment due to its location within the diatom belt and is influenced by the Antarctic Circumpolar Current mainly flowing west to east. Hydrothermal vent systems occur along the ESR, are characterized by nine tectonic segments (E1-E9). Sediment cores in the vicinity of ridge segments E2 and E9 from the ESR were analyzed to gain a better understanding of potential vent fluids related to trace metal distributions in surrounding modern marine sediments. Solid phase multicore and porewater samples collected during the R/V Polarstern Expedition PS_119 were located on both east and west sides of the ESR. Samples were selected at different distances from the hydrothermal vents along two west to east transects crossing E2 and E9 to gain a broader understanding of how chemical signatures within the sediment column change due to their proximity to the vents. As hydrothermally emitted plumes move throughout the water column, they affect where trace metals are deposit onto underlying sediments. Each core was analyzed using an inductively coupled plasma mass spectrometry. Analysis across the transects show a steady increase in trace metal concentrations on the eastern side of the ESR compared to samples from the western side indicating a currents-induced eastward movement of hydrothermal plumes from the ESR. In addition, sediments near E9 exhibited much higher trace metal enrichments compared to segment E2 signifying a more trace metal rich magmatic substrate source and different water-rock interactions increased metal concentrations within plumes and their deposits. Understanding the effects of hydrothermal activity on marine sediment is crucial when studying the productivity of an area using trace metal proxies because trace metal input from hydrothermal vents can overprint chemical signatures left from phytoplankton in marine sediments. Silver seems to be relatively unaffected by hydrothermal activity as it has similar concentrations within the cores analyzed, while cobalt and copper concentrations fluctuated with different distances from the hydrothermal vents. Thus, copper and cobalt have potential to indicate changes in deep ocean currents, while silver may be a good productivity proxy in the Southern Ocean.

TABLE OF CONTENTS

Chapter Page

LIST OF TABLES

Table Page

LIST OF FIGURES

CHAPTER I

INTRODUCTION

Tectonically active areas such as spreading ridges along plate boundaries are the primary places to find marine hydrothermal vents, where they can form alongside other hydrothermal vents to create a hydrothermal vent field (Tivey, 2007). Hydrothermal vents start with marine waters percolating inside the crust of the earth through cracks and porous rock. Once inside, the water or fluid is heated underneath by a heat source such as magma (Tivey, 2007, Hannington et al., 1986). With enough heat and pressure, these fluids become buoyant enough to be pushed out of the crust and into the water column (German et al., 2016, Tivey, 2007). These fissures are known as hydrothermal vents and the expelled fluids are hydrothermal plumes (Hannington et al., 1986).

There are many studies on trace metal concentrations and their behaviors within hydrothermal vent plumes and fluids (e.g., Metz & Trefry, 2000, James et al., 2014, Jacuot & Moffett, 2015), however, only a fraction focuses on the trace metal spatial distributions in modern marine sediments once they are deposited onto the seafloor from plumes (e.g., Agarwal et al., 2020). This study focuses on better understanding where productivity trace metals copper (Cu), cobalt (Co), and silver (Ag) are deposited in relation to the hydrothermal vent systems. This will be achieved by analyzing multicorer cores from different locations on and around the East Scotia Ridge (ESR) to delineate the magnitude of hydrothermal input influences on the sediment

column. The ESR is part of the diatom belt that results in large amounts of diatomaceous material deposited in marine sediments below 60°S as below this latitude, there are high numbers of diatoms in surface waters (Nissen et al., 2018). When these organisms die and their remains fall to the seafloor, a chemical biogenic signature in the sediments is left and can be analyzed to understand current and past productivity levels in the ESR region. However, these chemical productivity signatures might be overprinted by the hydrothermal activity in the region that produce high concentrations of trace metals. Documenting the extent, chemically and spatially of hydrothermal activity on geochemical proxies is essential to attain a higher accuracy and confidence in paleoproductivity studies.

1.1 Factors Controlling Hydrothermal Fluid Compositions

The composition of hydrothermal fluids is affected by biogenic processes, magmatic degassing, and phase separation (German & Von Damm, 2006). The effects of biogenic processes on vent fluids are still being studied and their affecting magnitudes are unknown; however, it is known that microbes can affect fluid compositions at temperatures below 120°C and influence H_2, H_2S, and CH_4 concentrations (German & Von Damm, 2006). Volatiles released into hydrothermal vent fluids are highly influenced by substrate mineralogy and water-rock interactions with seawater (Hannington et al., 1986, German & Von Damm, 2006). As such, the degassing of magma and vent fluids increase dissolved gasses such as SO_2, hydrogen sulfide (H_2S), and hydrofluoric acid concentrations in vent fluids which decrease pH values (around 3.3 for high temperature venting) and increase trace metal oxidation and solubility (Rogers et al., 2012, German & Von Damm, 2006, Metz & Trefry, 2000). These conditions, along with increasingly hot fluids leach surrounding rock and release more trace metals into hydrothermal fluids (German & Von Damm, 2006). An example of this can be seen in a study by Seyfried Jr. &

Ding, (1993) with an increase in dissolved Cu concentrations from 0.119-0.046 mmol/kg iron (Fe) (5.01-1.87 mmol/kg) and chlorine (Cl^-) (0.344-1.97 mol/kg) when pH increased from 4.79 to 5.0 in solution at 400ºC.

Hydrothermal processes form large quantities of chlorite that release Cl^- anions that are key for cation binding (German & Von Damm, 2006). Chlorine is highly conserved in hydrothermal systems (vent fluid changes of <6 to ~200% greater than seawater) because it is a product of the titration of HCO_3/CO_3 and the reduction/precipitation of sulfate (German & Von Damm, 2006). Thus, many chloro-complexes form in hydrothermal systems and can somewhat control major hydrothermal elements including cations such as calcium (Ca), Fe, and manganese (Mn) (German & Von Damm, 2006, Metz & Trefry, 2000, Rogers et al., 2012). Trace metals that bind with Cl^- severely increase their stability and metal mobilizations in hydrothermal fluids (Seewald & Seyfried Jr., 1990). The formation of these complexes can be impacted by rising temperatures which therefore increase the acidity of hydrothermal fluids by increasing surrounding minerals hydrous phases (Seewald & Seyfried Jr., 1990). Seyfried Jr. & Ding, (1992) found a relationship between more dissolved and mobile Fe (5.01 to 11.4 mmol/kg) and Cu (0.119 to 0.185 mmol/kg) particles in solution as Cl^- concentrations increased from 582 to 1570 mmol/kg and consequently, increased the amount of Cl^- anions available to complex with Fe and Cu.

1.2 Hydrothermal Plume and Particle Interactions and Depositions

Once outside the vent, fluid begin to pillow and rise upward while expanding from further seawater entrainments (German & Von Damm, 2006). Eventually, the plume reaches an equal buoyancy with the surrounding seawater and moves laterally outwards, until becoming heavily diluted with seawater and most of the particles (ranging from <10 to 500 μm) have fallen

out of suspension from particles combining with each other and become heavy enough to fall out of the plume (Hrischeva & Scott, 2007, Crocket, 1990). The more entrained and diluted a plume becomes, the more particles interact with oxygen rich seawater and each other and increase complexing and scavenging rates (German & Von Damm, 2006, Demina & Galkin, 2016). With more particles falling out of their plume, less remain inside the plume to be deposited at greater distances from venting sites. Thus, marine sediments will have less enrichments in trace metals and other particles as distances increase from hydrothermal sources. A study by Dymond and Roth, (1988) off the Endeavor Ridge, showed sediment particle fluxes decreased by a factor of 10-20 at distances further than 2 km away from near field particles that are relatively enriched in Fe and Cu (Hrischeva & Scott, 2007). The same principle applies to particles with different weights. A study by Hrischeva & Scott (2007) found that 90% of black smoker fine-grained material was deposited several hundred meters away from its substrate, while coarser-grained components were found within only a few hundred meters.

Despite this general trend of decreasing metal concentrations with increasing distances from the vent source, each metal has different transportation styles that lead to unique spatial distribution patterns in marine sediment (Hrischeva & Scott, 2007). Thus, hydrothermal sediment geochemical signatures also depend on seawater redox conditions and particle reactivity rates. As such, metals are generally deposited in corresponding order of their scavenging preferences (German & Von Damm, 2006). Near field sediment deposits reflect this with sulfides deposited closest to active vents, followed by Fe-Mn (oxy)hydroxides and silicates that form from low temperature diffusive vent fluid discharge, and lastly with precipitated fine-grained particles from hydrothermal plumes (Hrischeva & Scott, 2007, German & Von Damm, 2006). Near field deposits contain hydrothermal sediment closest to the vents and contain >90% of the fine-grained hydrothermal material in deposits up to 60 m away from active hydrothermal vents (German & Von Damm, 2006, Liao et al., 2018, Agarwal et al., 2020). Another component of hydrothermal

near field deposits are the weathering of sulfide mounds that are rich in minerals such as Fe rich chalcopyrite, as well as silicon (Si), and Cu within the inner layers of the mounds, and outer layers made up of sphalerite that contain higher concentrations of Ag and zinc (Zn) which are more mobile in lower temperatures (Zabel & Schulz, 2006, German & Von Damm, 2006). This generates an apron of detritus and metalliferous sediment that is rich in Mn and oxidized sulfides (German & Von Damm, 2006).

1.3 Types of Hydrothermal Vents

There are two kinds of hydrothermal vents. The first type, known as a white smoker, are characterized by their white expellant or smoke produced from venting silica-rich fluids with sporadic sulfide particles at temperatures less than 212ºC (Mills and Elderfield, 1995, Cole et al., 2014). These are typically enriched in Zn due to lower temperatures and have a pH lower than three (Edmond et al., 1995, Mills and Elderfield, 1995). The second type, black smokers produce oodles of sulfides (H2S) and metal rich particles such as Cu and Fe producing a discharge with a robust black color (Cole et al., 2014). These smokers typically have higher temperatures (350-400ºC) with pressures ranging from 350-450 bars at one to three kilometers (km) water depth that increase metal solubilities and concentrations within hydrothermal fluids (Crocket, 1990, Bohrmann et al., 2019, Seyfried Jr. & Ding, 1993). Both ridge segments E2 and E9 contain numerous black smokers (Bohrmann, 2019).

1.4 Productivity and Diatoms

Certain trace metals are known as essential micronutrients that influence productivity cycles especially in marine algae (Sunda, 1989). Metal uptake by phytoplankton is influenced by

several factors including the number of bioavailable metals available and the redox of surrounding seawater (Sunda, 1989). Once ingested, metals act as cofactors to form coordination complexes with different biomolecules like enzymes (Sunda, 1989). Some of these enzymes are used to catalyze important biological functions such as fixing carbon and photosynthesis (Cu, Fe, and Mn) (Plass et al, 2022). In high bio-essential metal abundant areas, some metals such as Cu can bond to the wrong metabolic site and act as an inhibitor, while others may be toxic (Sunda, 1989). Still, other metals such as Ag have no metabolic function, but are still ingested because of elevated concentrations (Sunda, 1989).

This primarily is attributed to phytoplankton such as diatoms adsorbing Ag into their soft tissues and skeletal components or frustules (Morford et al., 2008, Fisher and Wente, 1993, Wagner et al., 2022). Once deceased, frustules aggregate and sink through the water column at maximum sinking velocities of 70 m/day (Alldredge and Gotschalk, 1989, Passow, 1991, Fisher and Wente, 1993, Morford et al., 2008). The marine diatom *Thalassiosira weissflogii* is an example of this as it concentrates Ag in its cells at a range of 103.4 to 103.5 (volume/volume concentration) versus seawater with an average Ag concentration of 50 pM (Large et al., 2015, Kramer et al., 2011, Reinfelder and Sung, 1999). Diatoms also have traces of Fe (average of 9.255×10^{-14} g/cell), aluminum (Al), and slight enrichments of Cu (Fig. 8, Fig. 9) (Crosta et al., 2005, Burckle & Cirilli, 1987, Wagner et al., 2022). Richter (2013) found $Cu:Si_{Frustule}$ ratios ranging between 7.4×10^{-8} and 3.2×10^{-6} mol/mol in *Thalassiosira pseudonana* in the Southern Ocean (Wagner et al., 2022). These trace metal concentrations create chemical signatures in marine sediments from sinking diatomaceous matter that settle onto the seafloor and impact trace metal concentrations within the sediment column. This is especially true for diatoms below 60°S in the Southern Ocean as they account for 75% of the primary productivity in the diatom belt (Burckle & Cirilli, 1987, Nissen et al., 2018). Diatoms large abundance within surface waters also supplies sediments with copious amounts of siliceous material as they are rich in Si (average of

$1.09x10^{-12}$ g/cell) and contain specific amounts of trace metals (Crosta et al., 2005, Burckle & Cirilli, 1987, Crosta et al., 2005).

1.5 Trace Metals

Hydrothermal vents are major sources for metals including Co, Fe, Mn, Al, Ag, and Cu with Fe and Mn exceeding the input from rivers to the ocean (Table 1) (Agarwal et al., 2020). These metals derived from hydrothermal vents may be stabilized by organic complexes such as metal chelates and ligands (Kleint et al., 2022). Copper especially forms organic ligands as it is heavily chelated in seawater (Sunda, 1989). Often, organic complexes have high stability constants, allowing them to dominate the speciation of many trace metals in seawater and keep them in solution (Sander & Koschinsky, 2011). In hydrothermal areas, organic material may be sourced from the degradation of organic matter as well as by microbial activity (Kleint et al., 2022).

Table 1: Hydrothermal chemical fluxes of black smoker fluids and seawater for selected elements compared with chemical river fluxes to seawater (Elderfield & Schultz, 1996, Kadko et al., 1994).

Element	**Hydrothermal flux (10^{10} mol/year)**	**River flux (10^{10} mol/year)**
Fe	2.3-19	2.3
Mn	1.1-3.4	0.49
Ag	0.000078-0.000011	0.0088
Co	0.000066-0.00068	0.011
Cu	0.03-0.13	0.50
Al	0.012-0.06	6.0

Trace metals also form inorganic ligands with other metals such as Mn and Fe or as nanoparticles and sulfide complexations (Kleint et al., 2022, Sunda, 1989). In oxic seawater such

as in the Scotia Sea, both Fe-Mn-(oxy) hydroxides can serve as significant hosts for trace metals and sometimes their higher stability is preferred over sulfides during metal transportation within vent plumes (Abshire et al., 2020, Bruland and Lohan, 2006, Agarwal et al., 2020, Kleint et al., 2022). Often, these processes compete with organic complexation (Kleint et al., 2022). While in the water column, Fe and Mn scavenge trace metals that are subsequently deposited onto forming oxide crust from coprecipitation, replacement, and/or sorption (Schier, 2021). Copper and Fe sulfides are the first to be expelled and precipitated, followed by Mn and Fe oxides which settle at further distances (Agarwal et al., 2020). Generally, Mn becomes more dispersed in hydrothermal plumes where it is deposited at greater distances versus Fe, as Fe is more reactive and forms oxides quickly (Agarwal et al., 2020). This is due to Mn having different oxidation kinetics and becomes decoupled from Fe (Agarwal et al., 2020). An exception to this is nanoparticulate Fe that can be transported much further (Agarwal et al., 2020). High rates of chemical activity occur as metals are released from anoxic sediments and subsequently reprecipitated in oxic waters and deposited back onto the ocean floor (Plass et al, 2022). This can also happen with hydrothermal volatiles such as hydrogen sulfide that can become mobile within sediments when it interacts with oxidized, cold seawater (Kürzinger et al., 2022, Plass et al., 2022). Eventually, it leaves the seafloor and returns the bottom of the water column where it can then react with an oxidized metal and reprecipitate back onto the seafloor (Plass et al., 2022, Kürzinger et al., 2022). Near hydrothermal vents, these processes have little effect on sediments that receive continuous hydrothermal inputs and will generally have unchanged trace metal concentrations, allowing the preservation of their metalliferous signatures (Agarwal et al., 2020).

1.6 Silver (Ag)

Silver is toxic and a non-nutrient but exhibits a nutrient-like profile in the water column (Wagner et al., 2022). It has a higher accumulation in more reducing and acidic conditions, and therefore, tends to gather more in or below the oxygen minimum zone (McKay et al., 2008, Morford et al., 2008). A study conducted by Crusius and Thomson (2003) found that Ag immediately immobilized after oxidized Ag particles encountered reduced conditions in turbiditic sediments. In areas of high productivity there have been increases of Ag in sediment, linking Ag to productivity (Fisher and Wente, 1993). Hydrothermal vents and magmatic volatiles are another major source for Ag in marine deposits, its variability depends on factors such as source rocks and interactions from hydrothermal fluids and seawater (Keith et al., 2016, Williams-Jones & Heinrich, 2005). McKay et al. (2008) found Ag accumulations in marine sediments are best explained by particle scavenging in the water column. Additionally, Zang et al. (2004) proposed reversible scavenging as another mechanism for Ag being delivered into the sediment by re-scavenging processes from particles being released from dissolution. This latter mechanism may also be responsible for increased Ag concentrations at deeper seawater depths for deep water has fewer particles to scavenge Ag and lead to higher dissolved concentrations within seawater and higher accumulations within surface sediments (Abshire et al., 2020, Wagner et al., 2022). Martin et al. (1983) found values of 0.4 pmol/kg in surface waters, while 23 pmol/kg in deeper waters at 2300 meters (Bruland & Lohan, 2006). Since deep water has higher Ag concentrations, it follows that underlying surface sediments also have higher concentrations (Morford et al., 2008). A study by Morford et al. (2008), showed shallow water depths of <500 m contained the smallest Ag accumulation in sediments of <1 μmol/kg, while intermediate water depths of ~2000 m had intermediate Ag solid phase accumulations of 4-8 μmol/kg. This can be reflected into porewater as well, with higher concentrations related to the diffusion from the water column to the surface sediments or perhaps the release of degraded biogenic material (Abshire et al., 2020, Morford et

al., 2008). The mechanism of Ag sequestered in sediments is not well established. It has been proposed that the dissolution of biodetritus and Si carriers release bound Ag to bottom waters and the seafloor and through sulfide precipitation, which immobilizes and traps it in sediments (Crusius and Thomson, 2003, Wagner et al., 2022, Böning et al., 2004). This is supported by the fact that Ag prefers soft bases like sulfur that bind less effectively to protons and are polarizable (Wagner et al., 2022 Pearson, 1963).

1.7 Copper (Cu)

Copper is insoluble in reducing conditions and is only mobile in high temperatures (Little et al., 2017). The Cu^{2+} form is highly toxic even in low concentrations to phytoplankton (Little et al., 2017; Moffet & Brand, 1996). Yet in the water column, Cu behaves as a micronutrient and is depleted in surface waters while increasing its abundance with increasing depth in the water column (Sunda, 2012). Accordingly, Cu distributions correlate with other nutrients having a positive correlation with primary productivity and not with salinity (Saito et al., 2004, Steiner et al., 2017). This behavior, along with its high reactivity strongly influence its abundance in the ocean (Böning et al., 2004, Jacquot & Moffett, 2015). Thus, like Ag, it is depleted in surface seawater by extensive scavenging and subsequently sinks to deeper water (Jacquot & Moffett, 2015, Böning et al., 2004). Thus, Cu in the bottom water can act as a source for sediments, especially in oxygenated bottom water that mobilize Cu particles (Calvert & Pedersen, 1993). In a study by Calvert and Pederson (1993), porewater data showed that Cu is fixed at water depths below the oxygen minimum zone in anoxic sediments. Sander & Koshinsky (2011) found at hydrothermal vents; the oxidative dissolution of Cu sulfide particles leads to the formation of Cu organic ligands that then find their way to the anoxic-oxic transition zone. Ligands greatly

increase the stability of Cu, as such, most Cu (II) in near surface seawater is found as organic ligands (Steiner et al., 2017, Sunda, 1989).

In hydrothermal areas, scavenging is mainly with sulfides and Fe oxyhydroxides, and a smaller portion of very stable organic ligands that move further distances (Jacquot & Moffett, 2015). In seawater reducing conditions, Cu is insoluble and in hydrothermal fluids, it is thought to precipitate out quickly (Little et al., 2017). A study by Jacquot & Moffett (2015), demonstrated the difference in fluid concentrations from samples collected in a rising plume at heights from 200-350 m with concentrations of Cu^{2+} ranged from 4.48-6.5 fM, and ~0.5 pM taken directly from black smokers (Klevenz et al. 2012, Jacquot & Moffett, 2015). This difference was thought to be attributed to the increased time inside the rising plume, allowing for more scavenging and precipitation of sulfides and Fe oxyhydroxides (Jacquot & Moffett, 2015).

1.8 Cobalt (Co)

Cobalt behaves non-conservatively, similar to Fe, it has extremely low concentrations in seawater, especially in deeper waters (Saito et al., 2004, Viollier et al., 1995, Noble et al., 2012). Yet, at higher temperatures such as in hydrothermal vent fluids, it is more soluble than is augmented by Cl^- concentrations forming stabler complexes than with Cu (Swanner et al., 2014). Cobalt is dominated by organic complexation (over 90%), which make it harder for organisms to utilize (Saito et al., 2004, Bruland & Lohan, 2006). This causes an inverse relationship between Co in seawater and biological utilization (Saito et al., 2004). Unlike other nutrient type elements such as Ag, Co has a hybrid distribution profile in seawater with a scavenging behavior in intermediate to deep water (Noble et al., 2012, Wagner et al., 2022). This means that its main controls are its biological uptake and organic ligands that keep it depleted in surface water, while in deeper water it is scavenged and precipitated to the seafloor, making it also depleted in deeper

water (Bruland & Lohan, 2006, Noble et al., 2012). Organic ligands can transport Co to ocean sediments, but not efficiently (Swanner et al., 2014). Iron and Mn scavenging is the main transport for Co to reach the seafloor in oxygenated waters (Bruland & Lohan, 2006, Swanner et al., 2014). This is especially prevalent in hydrothermal areas such as the Scotia Sea where Co (II) and Co (III) are adsorbed onto Mn (II), Mn (III) and Fe (III) surfaces as their concentrations are several magnitudes higher than average seawater (Swanner et al., 2014, Noble et al., 2012). Once deposited, these complexes keep Co buried for long periods of time (Swanner et al., 2014).

Hydrothermal systems and water-rock interactions are major factors regarding oceanic Co concentrations (Swanner et al., 2014). However, Carr & Turekian, (1961) found that most Co in deep sea sediments resulted from detrital inputs from the surface runoff of streams. This follows because basaltic rocks contain much more Co (average of 48 ppm) than felsic rocks such as quartzite with an average concentration of only 0.3 ppm as Co prefers to form in ferromagnesian minerals (Carr & Turekian, 1961).

1.9 Study Area of The East Scotia Ridge

The Southern Ocean fully surrounds Antarctica and flows south of South America (Fig. 1). It also contains a smaller body of water called the South Scotia Sea. In this highly tectonically active area, the Scotia and Sandwich plates are diverging at rates between 60-70 km/Myr along the ESR, while the South American plate is subducting under the Sandwich plate at a rate of 70–85 km/Myr (Cole et al., 2014, Fretzdorff et al., 2002). Subduction of the South American plate has led to the creation of a volcanic island arc consisting of 11 main islands, the South Sandwich Trench, and the ESR (Fretzdorff et al., 2002, Leat et al., 2000, Cole et al., 2014). The Antarctic Circumpolar Current (ACC) runs in an easterly direction and just north of the East Scotia Ridge

(ESR), hitting its northernmost portion, then loops around South Georgia (Baker & Thomas, 2004,

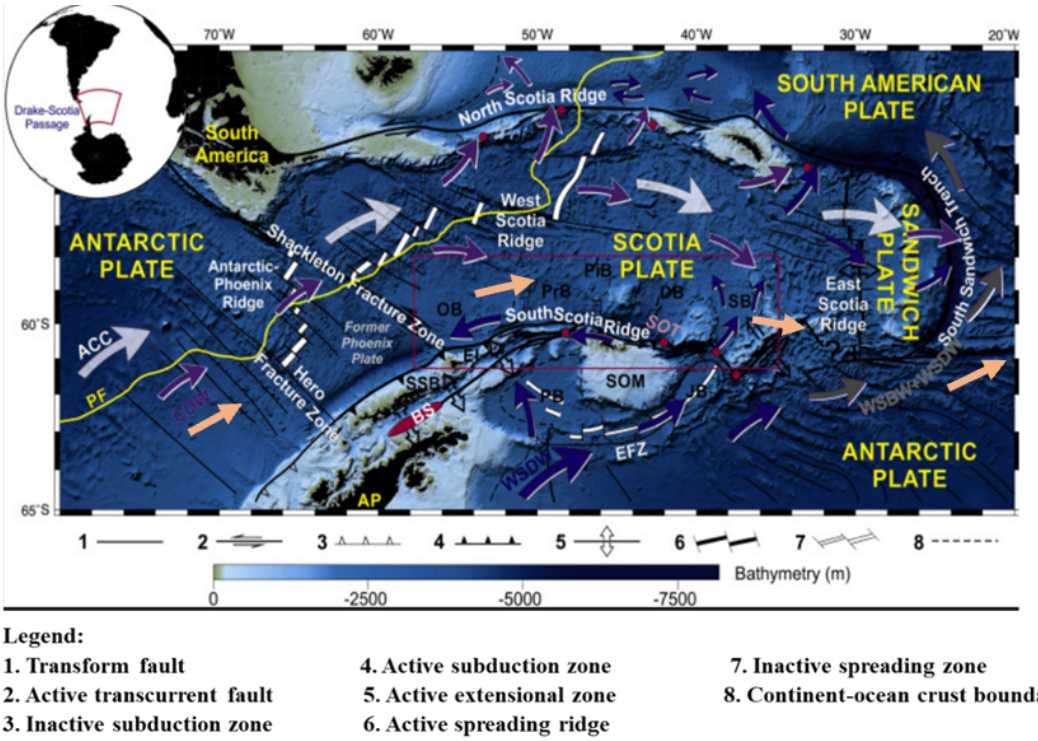

Legend:

1. Transform fault
2. Active transcurrent fault
3. Inactive subduction zone
4. Active subduction zone
5. Active extensional zone
6. Active spreading ridge
7. Inactive spreading zone
8. Continent-ocean crust boundary

Figure 1: Depiction of important features in the South Scotia Sea. The orange arrows indicate the diatom belt (Nissen et al., 2018), the white arrows indicate the directional flow of the Antarctic Circumpolar Current (ACC), while the purple arrows indicate the Circumpolar Deep Water (CDW) current flow, and the deep blue arrows indicate the directional flow of the Weddell Sea Deep Water (WSDW). Weddell Sea Bottom Water (WSBW), Antarctic Peninsula (AP), Bransfield Strait (BS), Dove Basin (DB), Pirie Basin (PiB), Endurance Fracture Zone (EFZ), South Orkney Trench (SOT), South Shetland Block (SSB), Protector Basin (PrB), Elephant Island (EI), Scan Basin (SB), Jane Basin (JB), South Orkney Microcontinent (SOM), South Orkney Trench (SOT), Ona Basin (OB), Powell Basin (PB) (Illustration modified from Pérez et al., 2019).

German et al., 2000). It is mainly driven by the South Hemisphere Westerlies between 45 and 55°S and, in most places, spans from the seafloor to the surface with generally decreasing velocities with depth (Sprenk et al., 2013). The current is also highly influenced by seafloor topography, where currents and plumes can trap particulate matter if the topography is higher than the plume (German et al., 1991).

The ESR is a back-arc hydrothermal system (Pereira, et al., 2022). Its proximity to the South Sandwich Island Arc postulates a strong influence from the South American Plate subduction on the underlying mantle (Fretzdorff et al., 2002, Livermore et al., 1997). Table 2 shows differences between fluid compositions from the ESR hydrothermal ridge segments E2 and E9 (Rodgers et al., 2012). The chemical differences in the vent plume fluids between these segments are partially the result of the ESR having heterogeneous magmatism from the subducting plate and differences in water-rock interactions (James et al., 2014, Fretzdorff et al., 2002, German & Von Damm, 2014, Rodgers et al., 2012). Both ridge segments have active black smokers that produce varying concentrations of trace metals (Cole et al., 2014). This study seeks to determine if the spatial distributions and concentrations of productivity trace metals Co, Ag, and Cu are distinct or similar around the vicinity of the ESR hydrothermal vent system.

The ESR is 500 km long and is made up of nine segments (E1-E9) that have been active at different times, starting around 15 million years ago (Fig. 2); these segments are separated by non-transform fault lateral offsets that move consistently (Fretzdorff et al., 2002, Cole et al., 2014, Leat et al., 2000, Rogers et al., 2012). Segments range compositionally from basalt to basaltic andesite (Fretzdorff et al., 2002). Ridge segments E3-E8 have deep and well-developed rift valleys, while segments E2 and E9 (Fig. 2) are unique and have axial topographically high volcanic ridges which result in faster than average magma production (Rogers et al., 2012, Leat et al., 2000). They also seem to be influenced more by the subducting slab by having more variable subduction components than the middle sections (Fretzdorff et al., 2002). This leads to increased magma production that inflates these segments with a melt lens below (Fretzdorff et al., 2002, Leat et al., 2000). It should be noted, that while seismically confirmed for segment E2, this is only hypothesized for E9 (Leat et al., 2000). These features are indicative of faster spreading ridges; however, because of the intermediate spreading rate of the ESR, increased magma production is thought to be the result of an easier to melt mantle (Leat et al., 2000, Fretzdorff et

al., 2002, Cole et al., 2014). According to Leat et al. (2000), this excess melting may be explained by higher quantities of volatiles released from subduction of the South American plate with a more hydrated mantle (Livermore et al., 1997). Increased magma production along with the presence of axial magma chambers and shallower melt lens below E2 and possibly E9 correlate to high temperature venting which increases metal uptake in vent fluids (Fretzdorff et al., 2002, Baker, 2009, German & Von Damm, 2006).

It is thought that the South American Plate is being torn eastward during its subduction (Fig. 3) (Leat et al., 2000). As tearing occurs, magma flows through it and around the edges of the South American Plate and contributes to the axial high of E2 (water depth of 2600 m) (Bohrmann, 2019, Cole et al., 2014, Leat et al., 2000). This magma flow is proposed to be the primary magma source for E2 (Fretzdorff et al., 2002, Leat et al., 2000). Figure 3 illustrates the tearing of the South American Plate during its subduction underneath the Sandwich Plate (Leat et al., 2000). Seismic data indicate that the inflation of E9 (water depth of 2400 m) is more complex than E2, as a collapsed magma body lies underneath E9 resulted from magma withdrawal (Bohrmann, 2019, Cole et al., 2014).

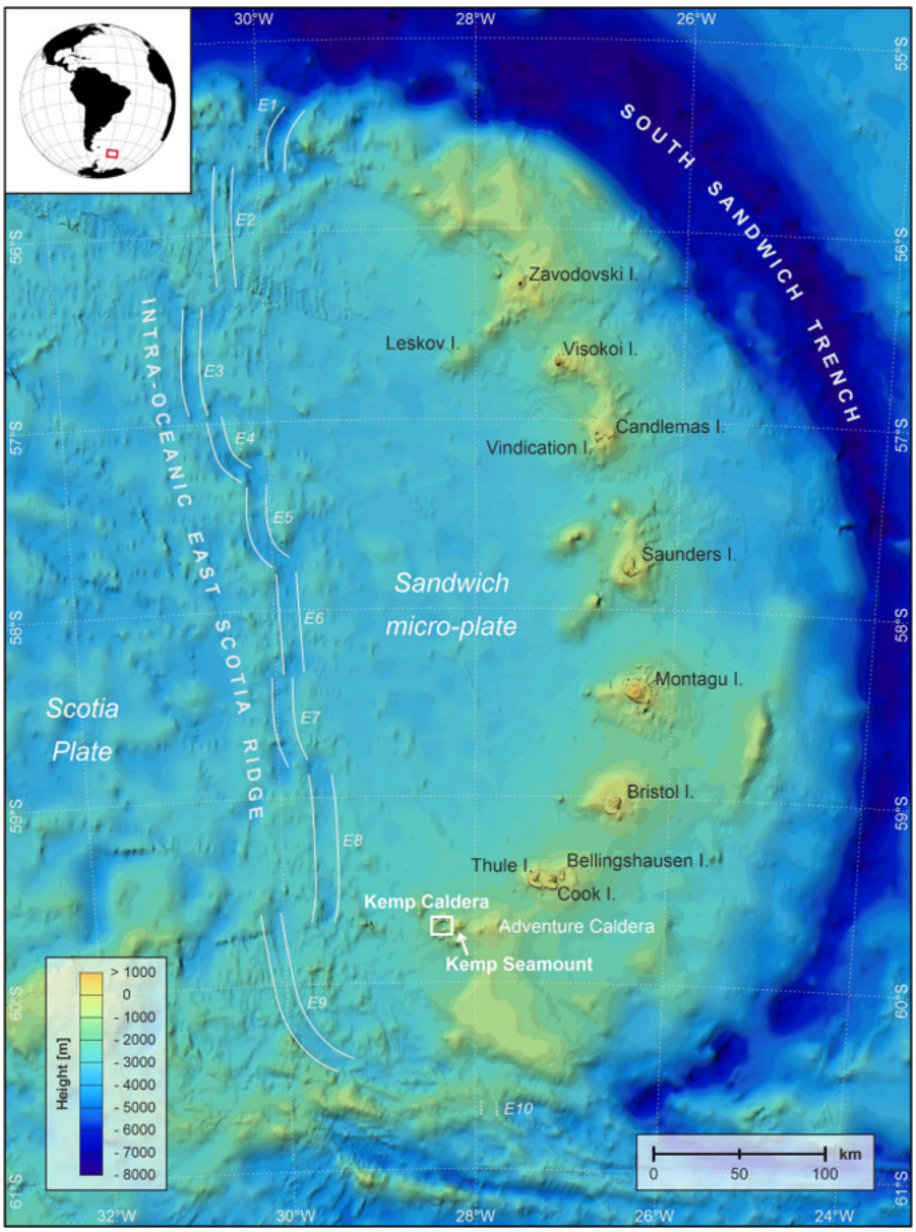

Figure 2: Illustration of the East Scotia Ridge segments and the Sandwich Micro-plate on a bathymetric map (Kürzinger et al., 2022). Ridge segments E2 and E9 are on opposite sides of the ESR and are 440 km apart, and Segment E9 is 90 km away from the Kemp Caldera (Bohrmann, 2019).

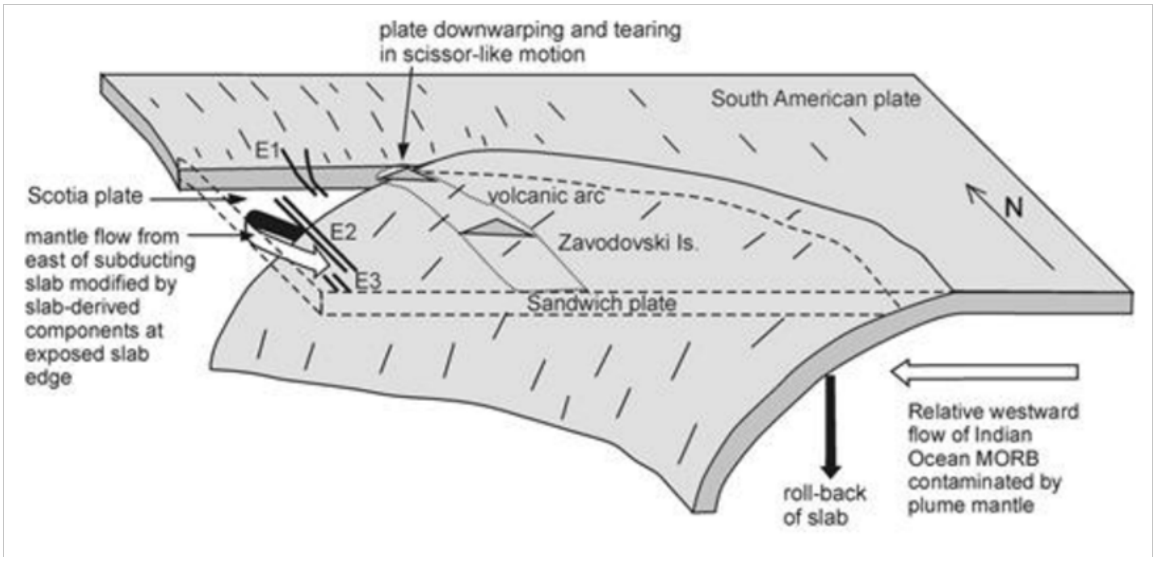

Figure 3: Depiction of the South American Plate (SAP) as it is being subducted underneath the Sandwich Plate (dashed lines). The flow of the mantle is shown by the white arrow as part of the SAP is being torn eastwards away from the rest of the plate. East Scotia Ridge segments are indicated above as E1, E2, and E3 (Leat et al., 2000).

Northern and southern sites of E9 have different hydrothermal fluid chemistries that Cole et al. (2014) attributed to the dissolution of lower subsurface temperature precipitates. These differ from fluid chemistries of E2 (Table 2) (Rogers et al., 2012). Site E2 has numerous active and extinct volcanic craters and cones (Bohrmann, 2019, Cole et al., 2014, German & Von Damm, 2006). While E9, contains more distinctive features like individual chimneys that are surrounded by flat sheet lavas, creating an extensive diffusive flow field for emitted plumes (Bohrmann, 2019, Cole et al., 2014, German & Von Damm, 2006). E9 is also subject to more magmatic material that heavily influences its vent fluid composition when compared to E2 and has more trace metals (Bohrmann, 2019). Both E9 and E2 segments have similar vent fluid temperatures of 351-353ºC at E2 and 348-383ºC at E9 (Cole et al., 2014, Bohrmann, 2019). The slightly higher temperatures of E9 increase metal solubility in hydrothermal fluids (German & Von Damm, 2006, Seewald & Seyfried Jr., 1990).

Located around segment E9, the submarine Kemp Caldera, ~65 km east of the ESR reaches depths of about 1600 m at the inner floor to 800-900 m at the rim of the caldera (Kürzinger et al., 2022). Here, hydrothermal fluids coexist with metal sulfides and elemental sulfur (S^0) that originate from fluids having a pH as low as <1 (Kürzinger et al., 2022, Cole et al., 2014). The cone surrounding the caldera and within it contain several white smokers and extinct chimneys with an increased pH of around 5.4 to 5.7 at 25°C (Kürzinger et al., 2022).

Table 2: Differences in the chemical compositions of hydrothermal vent fluids from ridge segments E2 & E9 end members (modified after Rogers et al., 2012). Data from the Atlantic (Schmidt et al., 2011), Indian (Gamo et al., 2001), and Pacific (Charlou et al., 1996) Oceans along with the mid-ocean ridges, back-arc basins (Fouquet, 1991, Craddock, 2009) are used for comparison to the ESR (Rogers et al., 2012).

Region	**Site**	**Maximum Temperature (°C)**	**Cl^- (mM)**	**pH**	**H_2S (mM)**	**Na (nmol/kg)**	**Si (mmol/ kg)**
ESR	E2	353	531	2.9	7.0	420	19
	E9N	383	98	3.4	9.5	96	8
	E9S	351	179	3.2	13.6	169	163
Mid-Ocean Ridges							
Atlantic Ocean	Nibelungen	372	567	2.9	1.1	449	13.7
Indian Ocean	Kairei	360	587	5.23		531	
Pacific Ocean	South East Pacific Rise	340	190	3	8.6	125	10.6
Back-Arc Basin	Lau Basin	334	650-800	2		520-615	14
	Pacmanus	341	625	2.6	6.3	495	17.8

CHAPTER II

METHODOLOGY

Sediment cores were collected from and near segments E2 and E9 from the ESR during cruise expedition PS_119 to the South Scotia Sea on the R/V Polarstern (Bohrmann, 2019). Multicore samples for solid phase analyses obtained subsurface depth penetration of 30 to 40 cm (Bohrmann, 2019). An exception to this was the push core sample from site 20-11. This sample was taken by using a remotely operated vehicle (ROV) collecting samples directly from the hydrothermal vent (appendix A1) (Bohrmann, 2019).

Porewater was extracted from MUC sediments on board the cruise expedition using Rhizons (0.15 μm average pore size) using sealed centrifuged tubes (Bohrmann, 2019, Seeberg-Elverfeldt et al., 2005). The first ml of extracted porewater for all samples was discarded to avoid any oxidation or contamination, and Fe was immediately analyzed on board using a DR Lange HACH 2800 photometer at a wavelength of 656 nm (Bohrmann, 2019). During Fe analysis, samples were pre-treated with 50 μl of ascorbic acid and then 50 μl of Ferrospectral solution to one ml aliquot of extracted porewater (Bohrmann, 2019). All other elements were analyzed at Oklahoma State University using an inductively coupled plasma-mass spectrometer (ICP-MS) Thermo Scientific iCAP Qc with Cetac autosampler.

Frozen sample splits (approximately 2-3 g) were taken from solid phase multicores for sample digestion. These splits were dried in an oven at 40°C for two to three days. Once dry, they

were crushed using an agate pestle and mortar and stored in glass vials. One hundred milligrams (mg) of each sample were weighed and added to Teflon vials and a sequence of three ml of trace metal grade HNO_3, two ml of $HClO_4$, and two ml of HF were added to each vial. Vials were heated to a boil on a hot plate for 10 hours. Samples were then removed from the hot plate and hooked up to an evaporation apparatus where they were heated for an additional 16.5 hours. Once cooled, 1.34 ml of 50% HNO_3 concentration were added to the sample vials and mixed until the samples dissolved. Then 8.66 ml of doubled-deionized water (Milli-Q) were added, and the vials were placed on a hot plate to be heated for another 2.5 hours. Once finished, these Teflon vials were removed from the hot plate and reweighted using an enclosed balance. After they were weighted, samples were poured into new, smaller vials and stored at room temperature. Next, samples were analyzed using an Agilent 7850ce inductively coupled plasma-mass spectrometry (ICP-MS) located at University of California-Riverside. Before analysis, they were diluted tenfold to nine ml of two percent HNO_3 for every one ml sample. All samples were handled using trace metal specific protocols to help eliminate the contamination and maximize the precision and accuracy of this study.

An FEI Quanta 600 field-emission gun Environmental Scanning Electron Microscope with a Bruker EDS X-ray microanalysis system and HKL EBSD system (SEM) imaged smear slides containing sediments from 14-2 at a depth of 14-17 cm at Oklahoma State University. Slides were created by placing sediment from the core onto a clean glass microscope slide. A few drops of deionized water were placed onto of the sediments to disperse them. They were then placed on a hot plate to evaporate all liquid. Once dried and cooled, an adhesive was applied on top of the sediments, followed by a glass cover. Care was taken to ensure the cover was airtight with no air bubbles and time was given to allow the adhesive to set.

Table 3: Samples were collected from ridge segments E2 and E9 from the East Scotia Ridge (ESR), while onboard Cruise PS-119 (PS_119). Samples were collected via a multi corer (MUC) and a manipulator arm with a sediment scoop-net (taken from Bohrmann, 2019).

Core name PS_119	**Vent location**	**Latitude (S)**	**Longitude (W)**	**Water depth (m)**	**Number of samples from core**
MUC-14-1	ESR-East E2	56º07.705’	30º04.176’	2763	13
MUC-15-2	ESR-East E2	56º06.598’	30º09.129’	3034	14
20-11 (Scoop)	ESR-E2 Vent fluid	56º05.3039’	30º19.1267’	2624	1
MUC-22-2	E2 West	56º09.316’	31º29.065’	3342	13
MUC-25-2	ESR-E9 West	59º52.743’	29º28.261’	2897	25
MUC-37-2	ESR-E8 East	59º29.187’	28º46.608’	2639	13
MUC-48-1	ESR-E2 East	56º21.208’	28º28.286’	2909	14

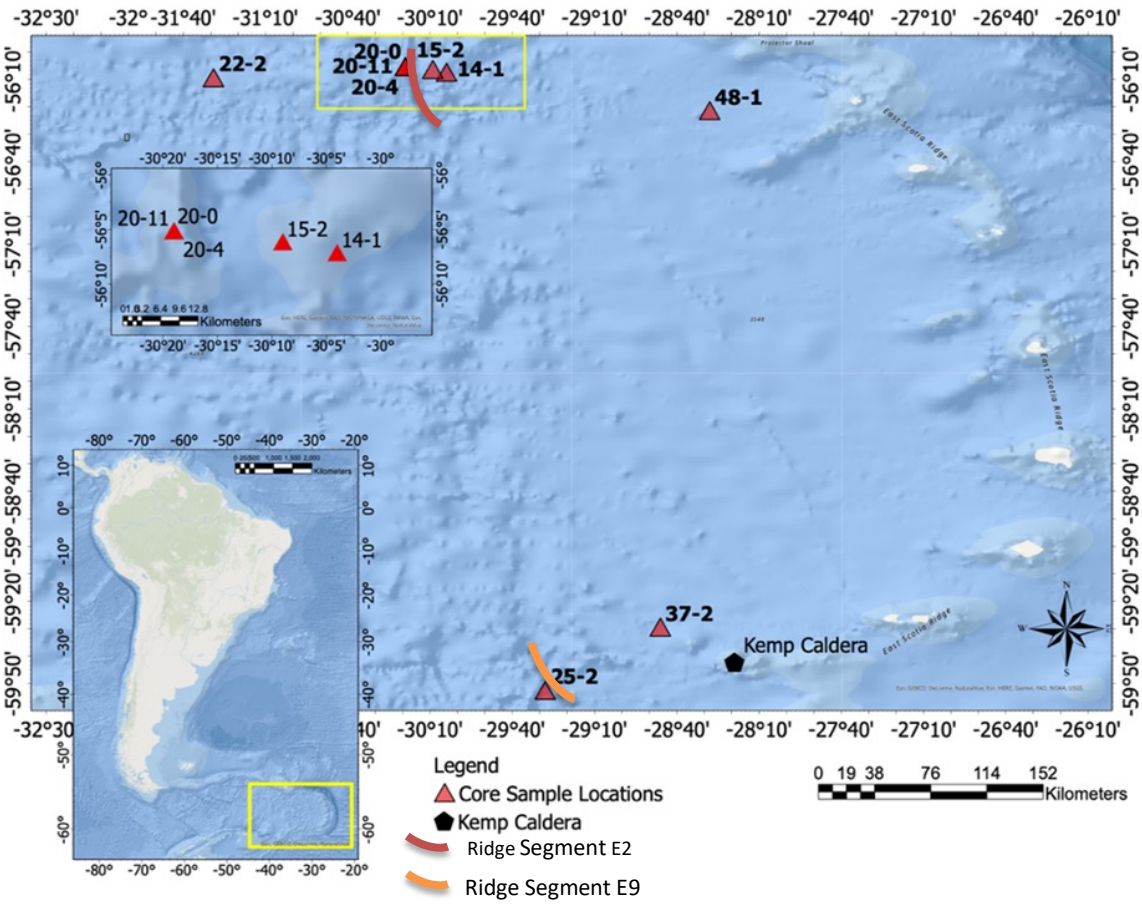

Figure 4: The triangles show the locations of where cores were collected within the South Scotia Sea. The exact location and number of core samples used for this study can be found in table 3.

CHAPTER III

RESULTS

3.1 Visual Core Descriptions

All cores are dominated by diatomaceous inputs throughout their entirety (Fig. 5) and are rich in Mn and Fe oxides leading to reddish to brown colored sediments. Core 22-2 is the furthest west from the ESR and is 32 cm long (Fig. 4). It has a thin layer of white fluffy diatomic ooze that is resting at the very top of the sediment surface. This is followed by nine cm of reddish-brown sediment with several cracks. The remaining part of the core is a beige brown color with reddish-brown interbedded layers within it. Core 15-2 is the closest to the hydrothermal venting and is 37 cm deep. It also has a filmy diatomic ooze layer (2-3 mm deep) overlying 10 cm of brown-red sediment with a lot of cracks. Underlying this layer, is another layer (14 cm long) that is whitish grey. A reddish layer follows this grey layer, which is on top of the bottom layer that is grey in color. The next closest core to 15-2 is 14-1 and is 31 cm long. It is followed by six cm of dark red sediments, followed by a beige layer. The dark red layer has small sized bits of beige particles that may be from the beige layer below it. This core also has a thin diatomaceous ooze on top. Core 48-1 has a slight layer of ooze on top of it. It is quite far from the hydrothermal vents located at E2 segment but is the closest to the South Sandwich Island Arc. It is 14 cm long and with a six cm layer of light brown sediment at the top followed by a 20 cm grey layer that increasingly gets darker closer to the bottom. As the core gets darker, it becomes sandier with

white inputs of potential volcanic glass. Core 37-2 has the thinnest layer of diatomaceous ooze that is proceeded by 27 cm of sediment, and a small eight cm layer of red brown sediment. These layers are underlain by a layer of 13 cm of grey sediments and followed by a 10 cm layer of a grey-red layer and an even darker grey layer at the very bottom. Core 25-2 has no diatomic ooze layer on top of it and is all a brownish red color in the upper 20 cm. The bottom of this core has laminations of lighter brownish red sediment with laminations of dark brown that may be clay.

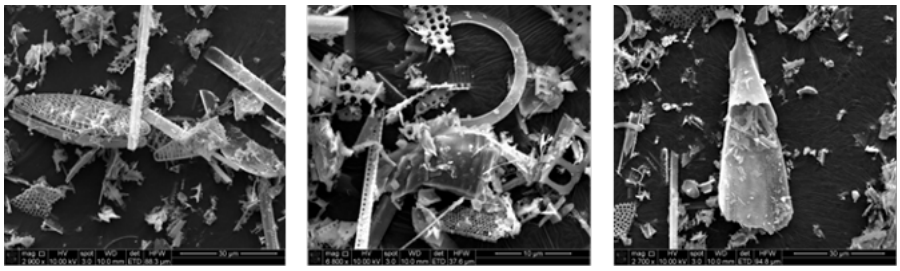

Figure 5: Scanning Electron Microscopy (SEM) images of the siliceous ooze found at depths of 14-17 cm in core 14-2. This ooze is representative of the siliceous ooze found within all MUCs analyzed.

3.2 Porewater

Iron for cores 25-2 and 15-2 were below the detection limit, while the highest average Fe concentration was from core 22-2 with an average of 5.41 μM (Table 4). Core 37-2 Fe porewater profile displays one large spike starting at eight cm with a concentration increase of 1.17 μM and increases down to 27 cm at 12.7 μM. Iron for 22-2 exhibited low concentrations of 0 and steadily increased to 39.63 μM at 32 cm deep (Fig. 7). Cores 14-1 and 15-2 displayed rather similar trends of increasing metal concentrations with increasing depths for most elements, particularly for Mn (0-28.6 μM, 0-50.0 μM) and Cu (10.28-128.95 nM, 6.95-126.46 nM) (Fig. 6). Core 25-2 also exhibits this trend with Mn ranging from 0.04-0.63 μM, and Cu ranging from 0-163.42 nM (Fig. 7). Copper shows an almost opposite trend to those of Co, Mn, and Fe which have very similar

profiles, core 37-2 is the exception to this as all three seem to increase towards the bottom of the core. Silver profiles seem independent and are largely constant, except for slight spikes around 5-10 cm in cores 15-2, 14-1, and 22-2. Core 15-2 had the largest average Ag concentration of 2.19 nM, while 48-1 had the lowest accumulation of Ag in its porewater of 0.49 nM and Cu with an average of 81.35 μM (Fig. 6, Fig. 7, Table 4). Yet, it also had the highest Co with an average of 23.37 nM (Table 4).

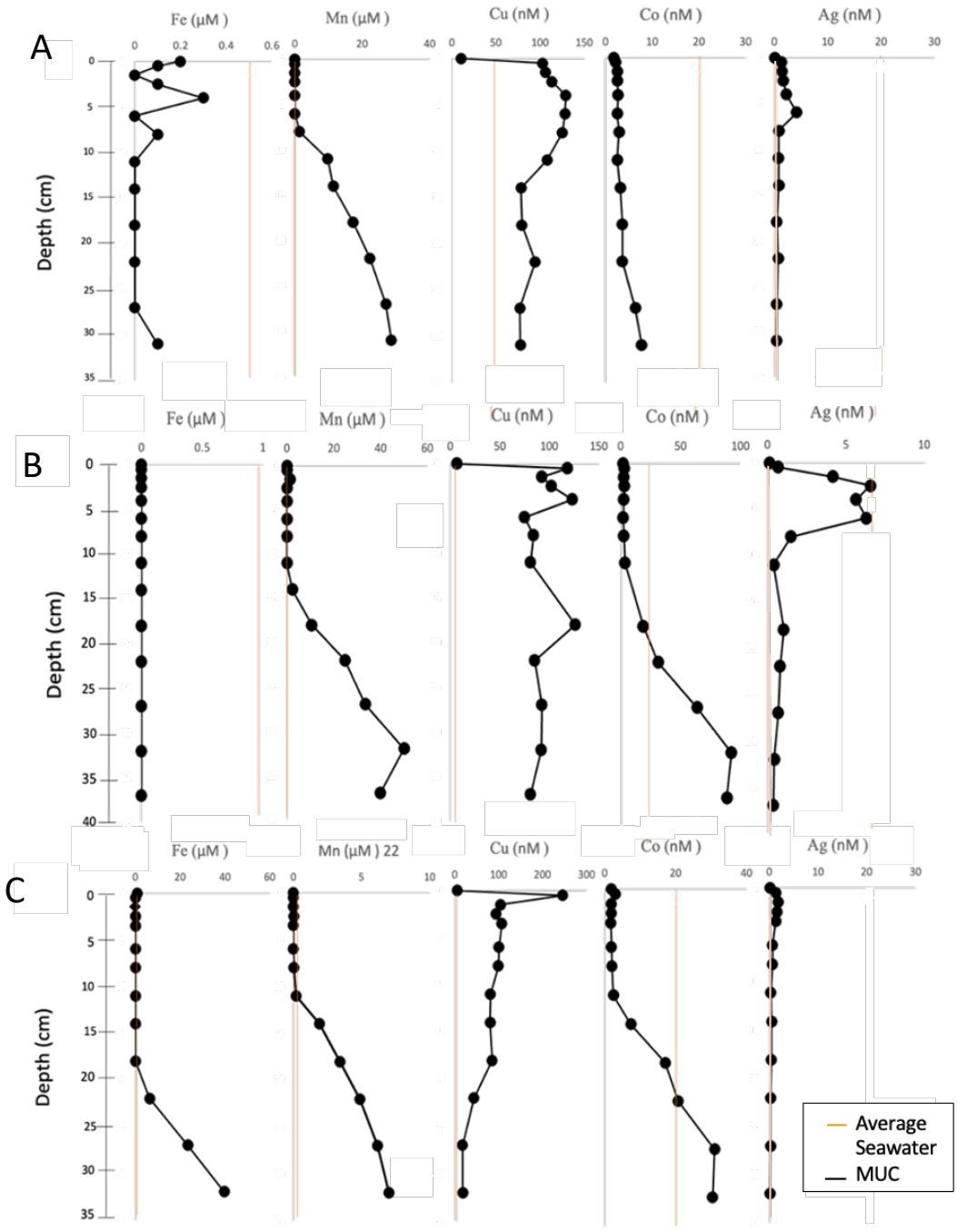

Figure 6: Porewater concentrations with increasing depths at the investigated sites 14-1 (A), 15-2 (B), and 22-2 (C). The orange line shows the average seawater concentration value (Bruland & Lohan, 2006).

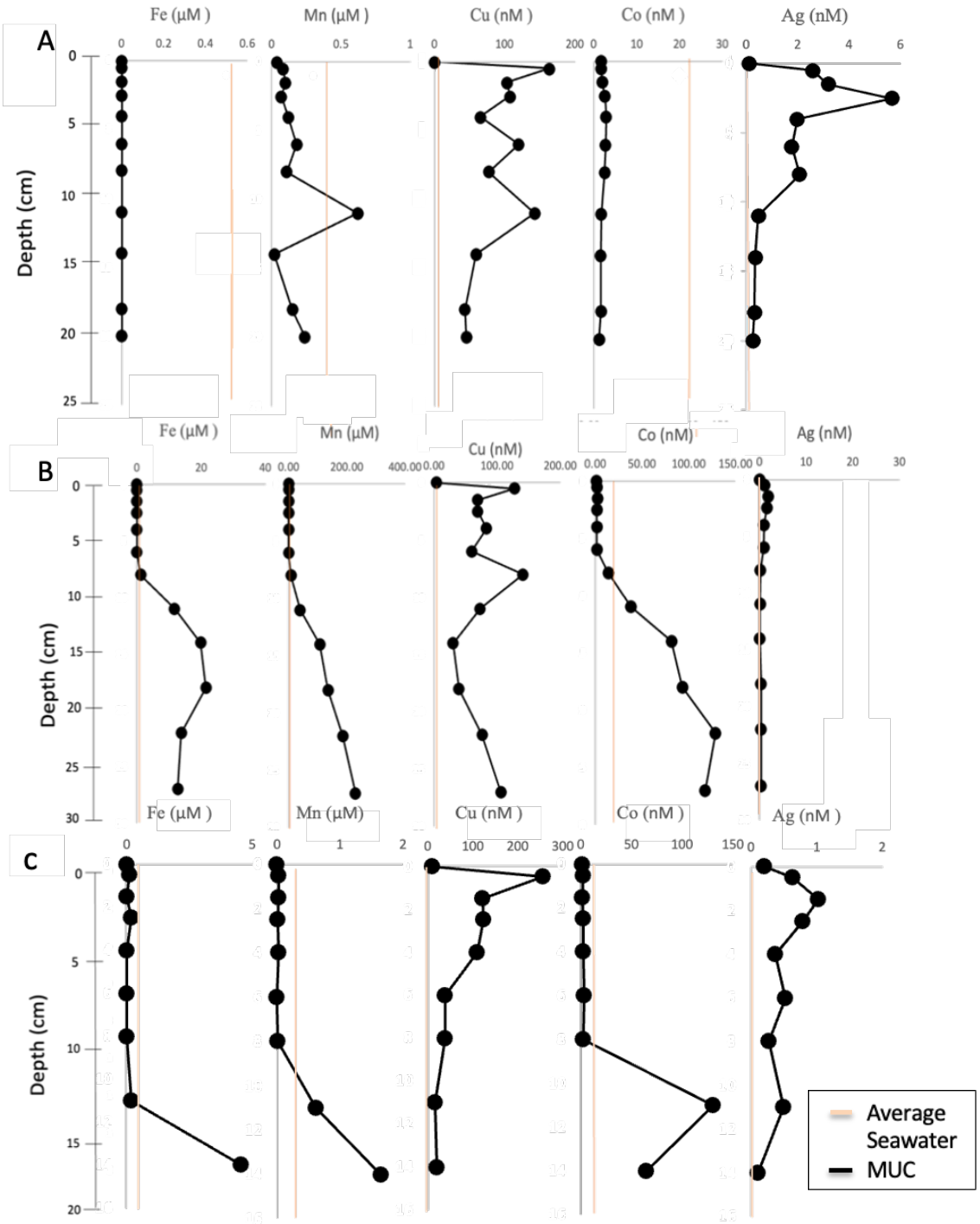

Figure 7: Porewater concentrations with increasing depths at the investigated sites 25-2 (A), 37-2 (B), and 48-1 (C). The dashed line shows the average seawater concentration value (Bruland & Lohan, 2006).

Table 4: Average values for aqueous samples collected at the ESR. See appendix A2 for list of all elemental concentrations.

Core number	Fe (µM)	Mn (µM)	Cu (nM)	Co (nM)	Ag (nM)
14-1	0.07	9.06	94.44	3.40	1.16
37-2	7.33	58.81	73.28	40.36	0.62
15-2	0.00	11.58	89.32	24.18	2.19
22-2	5.41	1.82	83.31	9.45	0.69
25-2	0.00	0.16	84.38	2.04	1.71
48-1	0.65	0.26	81.35	23.37	0.49

3.3 Solid Phase Cu, Fe, Mn, Ag, and Co

There seems to be an overall trend of cores having slight increases in trace metal concentrations on the eastern side of the ESR, and a much larger increase in concentrations at the E9 ridge segment. This is especially true for Mn at the southern end of the ESR at cores 25-2 with a concentration average of 3341 ppm and 37-2 with an average of 6149 ppm. E2 shows a similar behavior with a Cu average concentration of 161.80 ppm (37-2) compared to core 22-2 average of 57.88 ppm (Table 5). Both cores 37-2 and 25-2 exhibit similar elemental concentrations, however, 37-2 generally showed higher values for all elements of interest. Cores 22-2 and 48-2 are the sample endmembers of the W-E line of samples crossing over the E2 hydrothermal vent fields (Fig. 4). Cores 48-1 and 22-2 have very different solid phase profiles, while the middle cores, 14-1 and 15-2 exhibit characteristics of both endmembers (Fig. 7). There are also similarities between cores taken along the eastern portion of the ESR, cores 48-1 and 37-2. An example of this is both having consistently higher concentrations of Al of 7.20 wt% for core 48-1 and 6.62 wt% for core 37-2 versus core 22-2 having a wt% of 3.27 (Table 5). These east side

cores seem to have the most dissimilar trends with increasing depths and elemental concentrations. Other cores show the opposite and exhibit trends with each other as concentrations change with increasing corresponding depths. Sediment profiles follow porewater trends which did not have significant spikes in Ag, except within the first 5 cm. All cores except 14-1 showed a decreasing trend for Ag concentration with increasing sediment depth (Fig. 8).

Surface sediments from core 22-2 show a general decrease in concentrations with depth, except for Al (ranging from 2.97-3.69 wt%), which showed a slight increase (Table 5). Ag and Cu showed a rather large peak around 27 cm of 72.98 ppm before sharply decreasing to 38.95 ppm at 32 cm depth and Mn showed a large decrease in concentration at around 8 cm from 1130.7-299.5 ppm at 11 cm depth (Fig. 9). Cores 25-2, 15-2 and 14-1 are relatively similar with slight decreases in all metals (Fig. 8, Fig. 9). 14-1 did have a rather large general increase for Mn ranging from 1624.7-2768 ppm. Mn shows many fluctuations for all three cores as well as for core 37-2 (ranging 10483.9-2737.4 ppm); which also shows a rather large spike in Mn around 6 cm from 10483.9-14100.0 ppm. This is consistent with a change in sediment facies. Cores 48-1 and 25-2 also have many elements decreasing with depth except for Fe and Ag in core 48-1 (33289.8-40287.1 ppm for Fe and 0.293-0.286 ppm for Ag) and Mn (ranging 1394.2-2626.74 ppm) for the core 25-2 (Fig. 9).

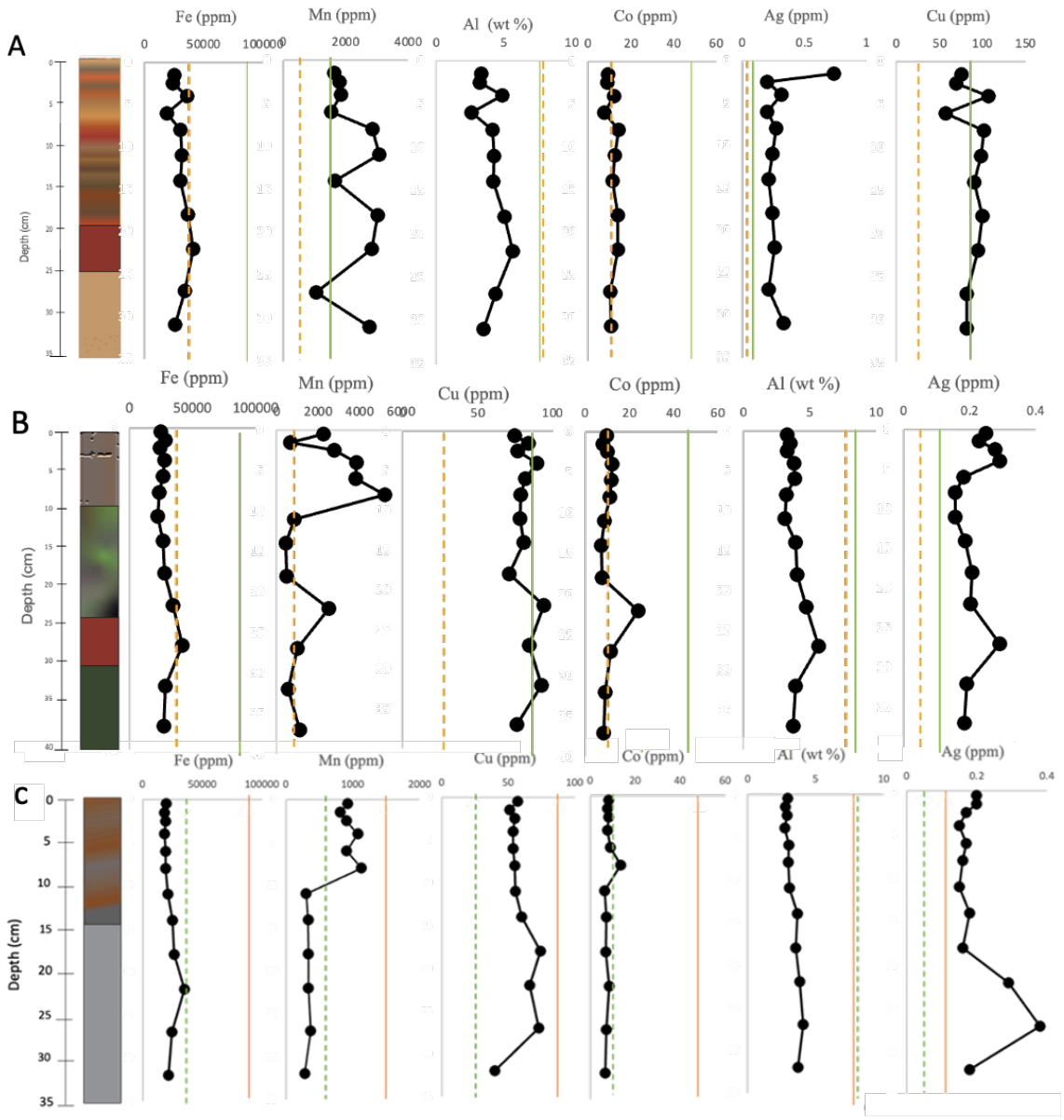

Figure 8: Solid phase concentration profiles for sites 14-1 (A), 15-2 (B), and 22-2 (C). The orange line represents typical basaltic rock compositions, and the smaller green dashed line represents the typical values of each element in the upper crust (Turekian & Wedepohl, 1961). Facies changes in sediment columns are shown by colored columns on the left side of the core profile. Core colors represent the true color and texture of each MUC (Bohrmann, 2019).

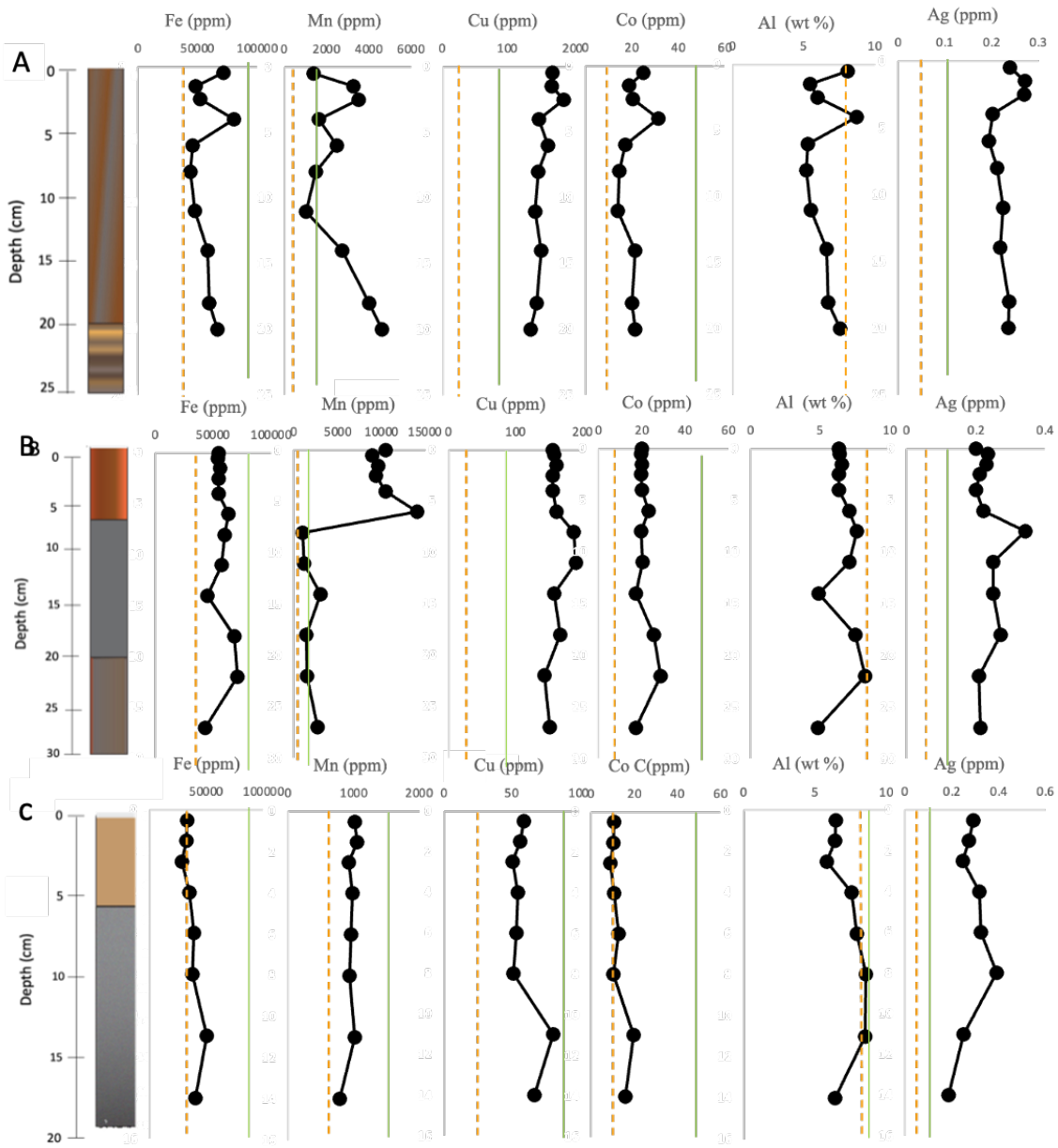

Figure 9: Solid phase concentration profiles for sites 25-2 (A), 37-2 (B), and 48-1 (C). The orange line represents typical basaltic rock compositions, and the smaller green dashed line represents the typical values of each element in the upper crust (Turekian & Wedepohl, 1961). Facies changes in sediment columns are shown by colored columns on the left side of the core profile. Core colors represent the true color and texture of each MUC (Bohrmann, 2019). the upper crust (Turekian & Wedepohl, 1961). Facies changes in sediment columns are shown by colored columns on the left side of the core profile. Core colors represent the true color and texture of each MUC (Bohrmann, 2019).

Table 5: Average values for solid phase samples collected at the East Scotia Ridge (ESR). Cores 25-2 and 37-2 are taken from sediments around E9. Both basaltic rock averages and upper crustal averages are taken from Turekian & Wedepohl (1961) for comparison with the enriched hydrothermal influenced sediments. See appendix A1 for all core elemental concentrations.

Core number	Al (wt%)	Fe (ppm)	Mn (ppm)	Cu (ppm)	Co (ppm)	Ag (ppm)
14-1	4.09	30403	2194	87.03	11.44	0.29
37-2	6.62	56768	6149	161.80	20.99	0.24
15-2	0.00	27993	1960	81.72	10.77	0.22
22-2	3.27	22366	642	57.88	8.09	0.20
25-2	6.52	57154	3341	155.47	20.52	0.23
48-1	7.20	37040	961	59.51	12.40	0.29
Basaltic Rocks	7.80	86500	1500	87.00	48.00	0.11
Upper Crust	8.04	35000	600	25.00	10.00	0.05

CHAPTER IV

DISCUSSION

Since the diatom belt runs through the ESR, multicores analyzed for this study contain copious amounts of diatomaceous material or ooze that is found throughout every core (Dutkiewicz, 2015). This includes the tops (except core 25-2), which contain visible diatomaceous material noted by a thin layer of white, fluffy film (Fig 5) (Bohrmann, 2019). Scanning Electron Microscopy (SEM) images were taken of core 14-1 to gain a better understanding of the chemical composition of the deposited siliceous material throughout the core (Fig. 5). It was found that the parts of the core analyzed did contain many diatom tests as well as other phytoplankton hard parts. However, sediment surrounding the ESR is very low in organic matter due to the highly oxic seawater (Reid et al., 2013, Sachs et al., 2009). Sachs et al, (2009) found that light C_{org} fluxes ranged from 3.3 $mgC/m^2/d$ to 3.9 $mgC/m^2/d$ in surrounding sediments closer to segment E9. This probably leads to very slight changes in trace metal concentrations within the sediment column.

4.1 Oxygen Penetration Zone

Due to a continuous flow of oxic seawater from the ACC and other local currents, sediment profiles of all multicores show deep zones of oxygen penetration of roughly 10 cm into

the sediment (Fig. 6, Fig. 7). This can be inferred from the Mn porewater profiles with Mn precipitating out of solution around this depth (Shaw et al., 1990). This deep penetration zone gives Mn a much greater influence on trace metal distributions throughout the sediment profiles compared to places with a more compressed Mn oxidant zone, that gives less room and time for Mn oxides to scavenge and accumulate metals within the sediment (Shaw et al., 1990). Preceding this zone, Mn oxides are further precipitated into the sediment column and accumulate with more reducing conditions (Shaw et al., 1990). This can be seen in the sediment profiles as Mn solid phase concentrations tend to increase with cores 25-2 and 37-2 in Fig. 9. Due to the large depth of the Mn oxidant zone, the Fe oxidant zone roughly starts around 25 to 35 cm and is barely visible at the bottom of only some of the multicores analyzed.

4.2 Solid Phase and Porewater Distributions of Cobalt

Within the Mn oxidant zone, Co shows high spikes in its concentration within all solid phase profiles. This is from Co being highly dependent on Mn concentrations as they are co-mobilized from the reductive dissolution of oxides within the sub-oxic zone (Zhou et al., 2020). Cores 15-2 and 22-2 are the best examples in this study of this, as they have very similar porewater profiles. Each show increases in their concentrations at the base of the oxygen penetration zone when they precipitate out of solution and accumulate deeper within the sediment profile (Fig. 6, Fig. 7). Once reductive dissolution occurs, they diffuse up within the sediment column to the oxic zone, where increased oxygen lead to Mn trapping Co quickly (Shaw et al., 1990). This leaves a trivial amount of Co to diffuse back into the water column. In areas with less oxygen, the rates of trapping Co by Mn oxides within the sediment decreases (Shaw et al., 1990). The small spikes found at the top of each profile represent the trapping of Co, and the overall cycling of Co with Mn within the sediment column. Cobalt has also been shown to remobilize

within the Fe oxidant, this may be seen slightly at the bottom of some of the deeper cores such as core 14-1 (Zhou et al., 2020).

Manganese and Co cycling in the sediment profile led to the assumption that both would have corresponding maximum concentrations at the same location, yet this is not the case. At segment E2, sediment averages show core 48-1 having the highest Co average of 12.40 ppm, while 14-1 had the highest accumulation for Mn at 2194 ppm. An explanation for this might stem from higher inputs of Co from another source. Swanner et al. (2014) has attributed some Co accumulations in marine sediments from terrestrial sources. Since 48-1 is much closer to the South Sandwich Island Arc, this offset might be attributed to small influxes of detrital sediment from the island arc. This would also explain the maximum Al content of 7.20 wt% at this site (14-1 had 4.09 wt%).

4.3 Solid Phase and Porewater Distributions of Copper

Copper has large enrichments in pore water profiles within the first 1-2 cm of each core. This peak stems from the reductive dissolution of Mn oxides and the upward diffusion of dissolved Cu throughout the sediment column (Shaw et al., 1990). At this depth, Cu concentrations accumulate near the water-sediment interface where Cu is both reprecipitated into oxic sediments or diffused into the water column from particle scavenging (Klinkhammer et al., 1982). It may also be attributed to a large sedimentation component outpacing Cu binding capacities with surrounding sediments that allow Cu to be scavenged back into the water column (Shaw et al., 1990). Klinkhammer et al. (1982) estimates that 90% of Cu escapes into the water column. However, due to such high Cu enrichments from hydrothermal vent fluids within underlying sediments as well as the overlying water column, Cu is maintained within the sediment column (Little et al., 2017, Klinkhammer et al., 1982). This is achieved from its high

binding capacity and reactivity with surrounding sediments that host many binding sites (Shaw et al., 1990). Thus, the top five cm within the sediment column has copious amounts of Cu recycling that is reflected by the various peaks found within the porewater profiles of this study. Copper also peaks at the oxic-suboxic boundary, this can be seen in the solid phase profiles of cores 37-2, 14-1, 48-1 (Shaw et al., 1990). This spike correlates relatively well to spikes in Mn and signify Cu recycling with Mn oxides. Overall, Cu shows a decreasing trend with increasing depth in porewater profiles (Fig. 7, Fig. 7), as anoxic sediments immobilize Cu and precipitate it out of solution (Little et al., 2017).

Copper also reacts with sulfides, sometimes without Fe due to its faster kinetics (Morse & Luther, 1999). Cores in this study increasingly show higher concentrations of Cu, closer to the vents, with Core 14-1 having the highest average concentration of 87.03 ppm. Core 15-2 is an exception and reported the second highest Cu average concentration of 81.72 ppm. This may be from a possible lag between near vent deposits and deposits of Cu transported further away.

4.4 Solid Phase and Porewater Distributions of Silver

The small peak in Ag concentration within the top few centimeters of the solid phase profiles suggest that Ag is controlled by the release of Fe and Mn oxides as well and is consequentially precipitated in the solid phase (Morford et al., 2008, Lyons & Fitzgerald, 1983). This is especially true given that Ag abundances are highest in bottom waters (Wagner et al., 2022). The release Ag from Mn and Fe (oxyhydr)oxides into porewater can be seen by a larger peak within the Mn and Fe oxidant zones of the sediment profiles (Morford et al., 2008). The solid phase profile of core 15-2 is a good example of this, as it shows a spike in concentration within both zones (Fig. 8). Like Co, the concentration of Ag is affected by the depth of the oxygen penetration zone (Shaw et al., 1990, Crusius & Thomson, 2003). The larger the zone, the

larger the upward flux of Ag. If this is coupled with an overlying water column that is exceedingly long, Ag sediments have an even larger flux (Morford et al., 2008). During burial within sediment profiles, Ag has been shown to immediately immobilize when contacting anoxic conditions (Crusius & Thomson, 2003). Thus, these conditions can lead to long term burial likely from the precipitation of the immobile elemental form of Ag and other immobile precipitants (Crusius & Thomson, 2003). Core 14-1 is a good example of this, with increasing concentrations at depth (Fig. 8). Porewater profiles show a different trend that is nearly linear, excluding the small spike at the top of the multicores (Fig. 6, Fig. 7). This is most likely due to a relatively unaffected change in concentrations within sediments, indicating that Ag is affected by a different source.

4.5 Influences of Current Direction on Lateral Trace Metal Distributions

Trace metal distributions were analyzed along a northern west-to-east transect across ridge segment E2, and a second southern one crossing segment E9 (Fig. 4). Each transect show relative increases in trace metal concentrations with increasing distance on the eastern side of the hydrothermal vent field compared to the western side (Tables 3 and 5). Lower average metal concentrations on the west side of the ESR are thought result from eastward flowing currents that move plumes with them and therefore, leave very little hydrothermal fluids to deposit on the western side of the ESR (Baker & Thomas, 2004).

Iron is the first major metal to react and precipitate out of vent fluids; German et al., 1991 suggested that most Fe is precipitated out of fluids mainly as Fe sulfides or Fe oxyhydroxides within a few hours of being erupted (Bruland & Lohan, 2006). Since near hydrothermal vent deposits generally contain sulfide deposits, followed by Mn and Fe oxyhydroxides, Fe should have relatively high concentrations within both deposits (Agarwal et al., 2020). However, Kleint

et al. (2022), reported a low ratio of 0.085 mM/mM for H_2S/Fe in hydrothermal fluids, signifying that a larger portion of Fe is precipitated with Fe oxyhydroxide formations instead of sulfides. In this study, similar trends are observed along the E2 transect (Fig. 4). Core 15-1 is the closest site to the vents and had the smallest average Fe concentration of 27993.1 ppm, while 48-1 contained the highest with a concentration of 37040 ppm and is the furthest away (Table 5). This means that it has a higher preference for depositing with sulfides versus Mn and Fe oxyhydroxides, reflecting its faster kinetics relative to Fe (Morse & Luther, 1999). The concentration of Ag does not change much along both transects (generally fluctuates between 0.2 and 0.3 ppm) delineating it is not well influenced from hydrothermal activity. This is unlike Cu and Co which show significant variations in concentrations and are much more influenced by the core sites proximity to hydrothermal activity. Copper has a spatial distribution with its highest average concentration in the sediment column at site 14-1 with 87.03 ppm, followed by a decrease in concentration further east at site 48-1 (59.51 ppm). While Co also has its highest average concentrations at site 14-1 of 11.44 ppm along the E2 transect. Contrarily, Co has a very high affinity for Mn and is often found together in sediments (Shae et al., 1990). A sample of hydrothermal fluid site 20-11 showed large enrichments in trace metals (Fe 28849 μM, Mn 27502 μM, Cu 9854.59 nM, Co 31.47 nM, Ag 7.03 nM), signifying that hydrothermal fluids are a significant source to trace metals to surrounding sediments. Aluminum is the exception as it is more controlled by detrital inputs, rather than hydrothermal (Bruland & Lohan, 2006). Site 48-1 is very close to the South Sandwich Island Arc and is speculated to have detrital inputs from these islands and lead to higher Co, Al, and Fe concentrations within sediments.

Garabato et al. (2001) proposed a local bottom water current that flows around the South Sandwich Island Arc starting from the southwestern side of the island arc and flowing northward, around the island arc and then back west across the ESR and segment E9 and the Kemp Caldera (Garabato et al., 2001). If this current does flow along this path, then hydrothermal fluids from

the Kemp Caldera would flow across E9 and potentially further enrich sediments with trace metals at sites 25-2 and 37-2. The current would also have the potential to slow down or move emitted vent plumes from E9 back across it and give underlying sediments more time to accumulate trace metals and help explain the higher trace metal enrichments found at cores along the E9 transect compared to the E2 transect.

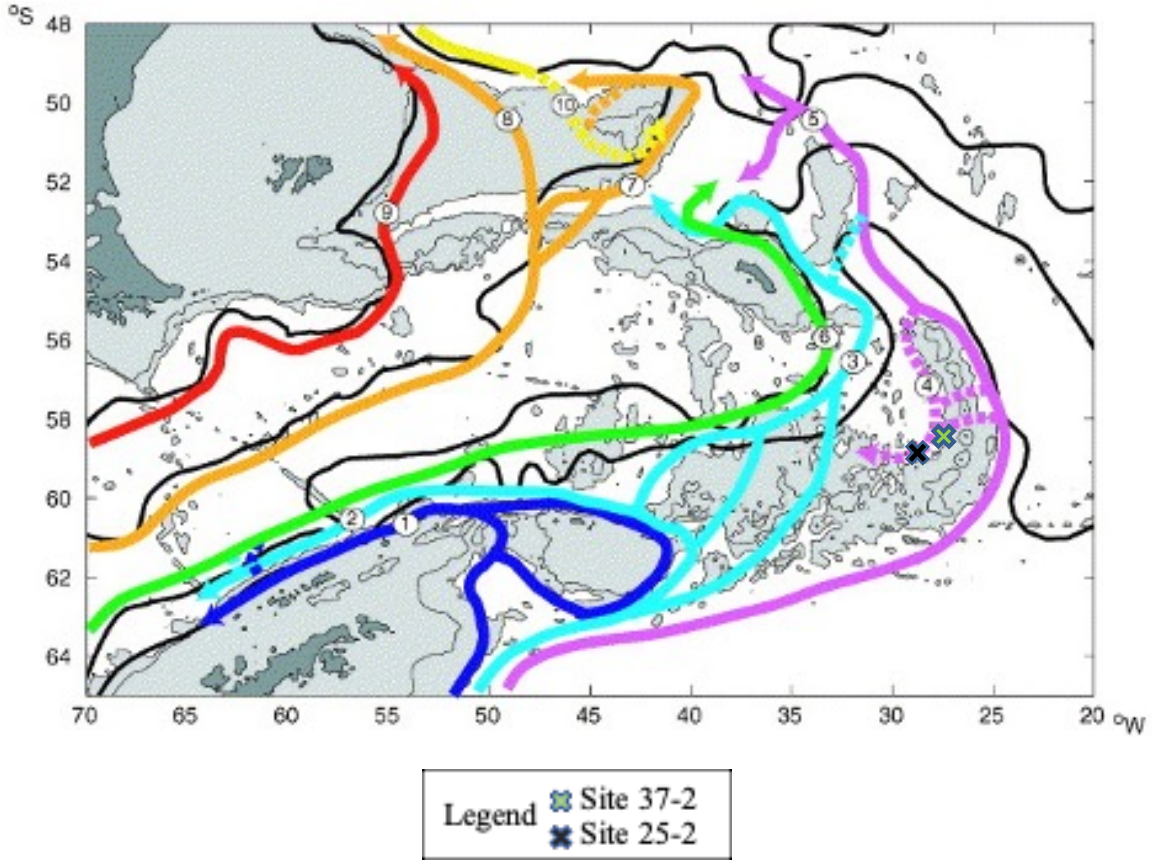

Figure 10: Colored pathways indicate different deep-water masses within the Scotia Sea. Dashed paths indicate unconfirmed or sporadic pathways. Note pathway four flows west across ridge segment E9 after passing through the South Sandwich Island Arc indicating possible backward movement of hydrothermal plumes that possibly increases trace metal concentrations in sediments relative to E2 (Modified after Garabato et al., 2002).

CHAPTER V

CONCLUSION

The waters along the ESR are very oxic, given the deep depths of the Mn oxidant zones followed by the Fe oxidant zone within the sediment column. The depths of these zones impact how trace metals are recycled within the sediment column. Silver, Co, and Cu show cycling within the sediment column by having enriched peaks at both the top and within the Mn oxidant zone, representing their association with Mn and Fe oxides that breakdown and become mobile in porewater from reductive dissolution, followed by the reprecipitation of oxides within the oxic zone. Cobalt correlates well with Mn within the sediment column as both show peaks relatively at the same depths (Fig. 6 & 7). Silver shows no increases in solid phase concentrations with depth or with changes in proximity to the hydrothermal venting, indicating its concentration is impacted by another source such as productivity. Copper shows a high level of activity in the upper five cm, particularly in porewater profiles. This behavior is likely the result of high Cu affinity for sediment bonding keeping Cu in the sediment. However, if there are not enough bonding sites, Cu is released back into the water column. This behavior is represented by a sharp decrease in porewater concentrations at the very top of each profile.

The sediment column surrounding segments E9 and E2 along the ESR show evidence of hydrothermal activity. Average concentrations of trace metals Ag, Co, Fe, Mn, and Cu in multicores have higher concentrations on the eastern side of the ridge than the western side. A

fluid sample taken directly from a hydrothermal vent had the highest concentrations of all samples analyzed and signifies the influence of hydrothermal activity on trace metal depositions. This is especially true as local currents, particularly the ACC move vent plumes east of the ESR that lead to larger hydrothermal impacts on sediments east of the ridge due to plume fallout. Segment E9 seems to be impacted by a richer magmatic source with different water-rock interactions that differentiate the trace metal averages from those found at the E2 transect.

The importance of understanding where and how these trace metals are deposited in relation to hydrothermal vents gives a better understanding on the behavior of trace metals in hydrothermal fluids, their transport through plumes, as well as mechanisms controlling their spatial distribution in sediments. The findings of this study emphasize the need of considering the environmental surroundings of a study site to eliminate potential overprinting of productivity signatures in the Southern Ocean due to is unchanging depositional concentration on both the east and western side of the ESR, as well with depth through the sediment column. This is unlike Cu and Co which change dramatically with changes in distance from hydrothermal vents. However, these metals might be good proxies for studying local bottom water currents as the currents move with hydrothermal plumes in the water column.

REFERENCES

Abshire, M. L., Owens, J. D., Cofrancesco, J., Inthorn, M., & Riedinger, N. (2020). Geochemical signatures of redepositional environments: The Namibian continental margin. Marine Geology, 429, 106316.

Agarwal, D. K., Roy, P., Prakash, L. S., & Kurian, P. J. (2020). Hydrothermal signatures in sediments from eastern Southwest Indian Ridge 63 E to 68 E. Marine Chemistry, 218, 103732.

Alldredge, A. L., & Gotschalk, C. C. (1989). Direct observations of the mass flocculation of diatom blooms: characteristics, settling velocities and formation of diatom aggregates. Deep Sea Research Part A. oceanographic research Papers, 36(2), 159-171.

Baker, E. T. (2009). Relationships between hydrothermal activity and axial magma chamber distribution, depth, and melt content. Geochemistry, Geophysics, Geosystems, 10(6).

Barker, P. F., & Thomas, E. (2004). Origin, signature and palaeoclimatic influence of the Antarctic Circumpolar Current. Earth-Science Reviews, 66(1-2), 143-162.

Bohrmann, G. (2019). The expedition PS119 of the research vessel Polarstern to Eastern Scotia Sea in 2019.

Böning, P., Brumsack, H. J., Böttcher, M. E., Schnetger, B., Kriete, C., Kallmeyer, J., & Borchers, S. L. (2004). Geochemistry of Peruvian near-surface sediments. Geochimica et cosmochimica acta, 68(21), 4429-4451.

Bruland, K. W., & Lohan, M. C. (2006). Controls of trace metals in seawater. The oceans and marine geochemistry, 6, 23-47.

Burckle, L. H., & Cirilli, J. (1987). Origin of diatom ooze belt in the Southern Ocean; implications for late Quaterary paleoceanography. Micropaleontology, 33(1), 82-86.

Calvert, S. E., & Pedersen, T. F. (1993). Geochemistry of recent oxic and anoxic marine sediments: implications for the geological record. Marine geology, 113(1-2), 67-88.

Carr, M. H., & Turekian, K. K. (1961). The geochemistry of cobalt. Geochimica et Cosmochimica Acta, 23(1-2), 9-60.

Charlou, J. L., Fouquet, Y., Donval, J. P., Auzende, J. M., Jean-Baptiste, P., Stievenard, M., & Michel, S. (1996). Mineral and gas chemistry of hydrothermal fluids on an ultrafast spreading ridge: East Pacific Rise, 17 to 19 S (Naudur cruise, 1993) phase separation processes controlled by volcanic and tectonic activity. Journal of Geophysical Research: Solid Earth, 101(B7), 15899-15919.

Cole, C. S., James, R. H., Connelly, D. P., & Hathorne, E. C. (2014). Rare earth elements as indicators of hydrothermal processes within the East Scotia subduction zone system. Geochimica et Cosmochimica Acta, 140, 20-38.

Craddock, P. R. (2009). Geochemical tracers of processes affecting the formation of seafloor hydrothermal fluids and deposits in the Manus back-arc basin. MASSACHUSETTS INST OF TECH CAMBRIDGE.

Crocket, J. H. (1990). Noble Metals in seafloor hydrothermal mineralization from the Juan de Fuca and Mid-Atlantic ridges; a fractionation of gold from platinum metals in hydrothermal fields. The Canadian Mineralogist, 28(3), 639-648.

Crosta, X., Romero, O., Armand, L. K., & Pichon, J. J. (2005). The biogeography of major diatom taxa in Southern Ocean sediments: 2. Open ocean related species. Palaeogeography, Palaeoclimatology, Palaeoecology, 223(1-2), 66-92.

Crusius, J., & Thomson, J. (2003). Mobility of authigenic rhenium, silver, and selenium during postdepositional oxidation in marine sediments. Geochimica et Cosochimica Acta, 67(2), 265-273.

Demina, L. L., & Galkin, S. V. (Eds.). (2016). Trace metal biogeochemistry and ecology of deep-sea hydrothermal vent systems (Vol. 50). Springer.

Dutkiewicz, A., Müller, R. D., O'Callaghan, S., & Jónasson, H. (2015). Census of seafloor sediments in the world's ocean. Geology, 43(9), 795-798.

Dymond, J., & Roth, S. (1988). Plume dispersed hydrothermal particles: a time-series record of settling flux from the Endeavour Ridge using moored sensors. Geochimica et Cosmochimica Acta, 52(10), 2525-2536.

Edmond, J. M., Campbell, A. C., Palmer, M. R., Klinkhammer, G. P., German, C. R., Edmonds, H. N., Elderfield, H., Thompson, G., & Rona, P. (1995). Time series studies of vent fluids from the TAG and MARK sites (1986, 1990) Mid-Atlantic Ridge: a new solution chemistry model and a mechanism for Cu/Zn zonation in massive sulphide orebodies. Geological Society, London, Special Publications, 87(1), 77-86.

Elderfield, H., & Schultz, A. (1996). Mid-ocean ridge hydrothermal fluxes and the chemical composition of the ocean. Annual Review of Earth and Planetary Sciences, 24, 191-224.

Fisher, N. S., & Wente, M. (1993). The release of trace elements by dying marine phytoplankton. Deep Sea Research Part I: Oceanographic Research Papers, 40(4), 671-694.

Flegal, A. R., Sanudo-Wilhelmy, S. A., & Scelfo, G. M. (1995). Silver in the eastern Atlantic Ocean. Marine Chemistry, 49(4), 315-320.

Fretzdoff, S., Livermore, R. A., Devey, C. W., Leat, P. T., & Stoffers, P. (2002). Petrogenesis of the back-arc east scotia ridge, south Atlantic Ocean. Journal of Petrology, 43(8), 1435-1467.

Fouquet, Y., von Stackelberg, U., Charlou, J. L., Donval, J. P., Foucher, J. P., Erzinger, J., Herzig, P., Muhe, R., Wiedicke, M., Soakai, S., & Whitechurch, H. (1991). Hydrothermal activity in the Lau back-arc basin: Sulfides and water chemistry. Geology, 19(4), 303-306.

Gamo, T., Chiba, H., Yamanaka, T., Okudaira, T., Hashimoto, J., Tsuchida, S., Ishibashi, J., Kataoka, S., Tsunogai, U., Oklamura, K., Sano, K., & Shinjo, R. (2001). Chemical characteristics of newly discovered black smoker fluids and associated hydrothermal plumes at the Rodriguez Triple Junction, Central Indian Ridge. Earth and Planetary Science Letters, 193(3-4), 371-379.

Garabato, A. C. N., Heywood, K. J., & Stevens, D. P. (2002). Modification and pathways of Southern Ocean deep waters in the Scotia Sea. Deep Sea Research Part I: Oceanographic Research Papers, 49(4), 681-705.

German, C. R., Campbell, A. C., & Edmond, J. M. (1991). Hydrothermal scavenging at the Mid-Atlantic Ridge: Modification of trace element dissolved fluxes. Earth and Planetary Science Letters, 107(1), 101-114.

German, C. R., Casciotti, K. A., Dutay, J. C., Heimbürger, L. E., Jenkins, W. J., Measures, C. I., Mills, R. A., Obata, H., Schlitzer, R., Tagliabue, A., Turner, D. R., & Whitby, H. (2016). Hydrothermal impacts on trace element and isotope ocean biogeochemistry. Philosophical Transactions of the Royal Society A: Mathematical, Physical and Engineering Sciences, 374(2081), 20160035.

German, C. R., Livermore, R. A., Baker, E. T., Bruguier, N. I., Connelly, D. P., Cunningham, A. P., Morris, P., Rouse, I. P., Statham, P. J., & Tyler, P. A. (2000). Hydrothermal plumes above the East Scotia Ridge: an isolated high latitude back-arc spreading centre. Earth and Planetary Science Letters, 184(1), 241-250.

German, C. R., & Von Damm, K. L. (2006). Hydrothermal processes. Treatise on geochemistry, 6, 181-222.

González-Santana, D., González-Dávila, M., Lohan, M. C., Artigue, L., Planquette, H., Sarthou, G., Tagliabue, A., & Santana-Casiano, J. M. (2021). Variability in iron (II) oxidation kinetics across diverse hydrothermal sites on the northern Mid Atlantic Ridge. Geochimica et Cosmochimica Acta, 297, 143-157.

Hawkes, J. A., Connelly, D. P., Rijkenberg, M. J., & Achterberg, E. P. (2014). The importance of shallow hydrothermal island arc systems in ocean biogeochemistry. Geophysical Research Letters, 41(3), 942-947

Hannington, M.D., Peter, J. M., & Scott, S. D. (1986). Gold in sea-floor polymetallic sulfide deposits. Economic Geology, 81(8), 1867-1883.

Hoefs, J., & Hoefs, J. (1997). Stable isotope geochemistry (Vol. 201). Berlin: Springer.

Hrischeva, E., & Scott, S. D. (2007). Geochemistry and morphology of metalliferous sediments and oxyhydroxides from the Endeavor segment, Juan de Fuca Ridge. Geochimica et Cosmochimica Acta, 71(14), 3476-3497.

Jacquot, J. E., & Moffett, J. W. (2015). Copper distribution and speciation across the International GEOTRACES Section GA03. Deep Sea Research Part II: Topical Studies in Oceanography, 116, 187-207.

James, R. H., Green, D. R., Stock, M. J., Alker, B. J., Banerjee, N. R., Cole, C., German, C, R., Huvenne, V. A.I., Powell, A. M., & Connelly, S. P. (2014). Composition of hydrothermal fluids and mineralogy of associated chimney material on the East Scotia Ridge back-arc spreading centre, Geochimica et Cosmochimica Acta, 139, 47-71.

Jickells, T. D., An, Z. S., Andersen, K. K., Baker, A. R., Bergametti, G., Brooks, N., Cao, J. J., Boyd, P. W., Duce, R. A., Hunter, K. A., Kawahata, H., Kubilay, N., Laroche, J., Liss, P, S., Mahowald, N., Prospero, J. M., Ridgwell, A. J., Tegen, I., & Torres, R. (2005). Global iron connections between desert dust, ocean biogeochemistry, and climate. science, 308(5718), 67-71.

Kadko D., Baker E. T., Alt, J., Baross, J., 1994. Global impact of submarine hydrothermal processes. Final Rep. Ridge/Vent Workshop. 55 pp.

Keith, M., Häckel, F., Haase, K. M., Schwarz-Schampera, U., & Klemd, R. (2016). Trace element systematics of pyrite from submarine hydrothermal vents. Ore Geology Reviews, 72, 728-745.

Klevenz, V., Sander, S. G., Perner, M., & Koschinsky, A. (2012). Amelioration of free copper by hydrothermal vent microbes as a response to high copper concentrations. Chemistry and Ecology, 28(5), 405-420.

Kormas, K. A., Tivey, M. K., Von Damm, K., & Teske, A. (2006). Bacterial and archaeal phylotypes associated with distinct mineralogical layers of a white smoker spire from a deep-sea hydrothermal vent site (9°N, East Pacific Rise). Environmental Microbiology, 8(5), 909-920.

Kramer, D., Cullen, J. T., Christian, J. R., Johnson, W. K., & Pedersen, T. F. (2011). Silver in the subarctic northeast Pacific Ocean: Explaining the basin scale distribution of silver. Marine Chemistry, 123(1-4), 133-142.

Kleint, C., Zitoun, R., Neuholz, R., Walter, M., Schnetger, B., Klose, L., Chriswell, S. M., Middag, R., Lann, P., Sander, S., & Koschinsky, A. (2022). Trace metal dynamics in shallow hydrothermal plumes at the Kermadec arc. Frontiers in Marine Science, 8, Art-Nr.

Klinkhammer, G., Heggie, D. T., & Graham, D. W. (1982). Metal diagenesis in oxic marine sediments. Earth and Planetary Science Letters, 61(2), 211-219.

Kürzinger, V., Diehl, A., Pereira, S. I., Strauss, H., Bohrmann, G., & Bach, W. (2022). Sulfur formation associated with coexisting sulfide minerals in the Kemp Caldera hydrothermal system, Scotia Sea. Chemical Geology 606, 120927.

Large, R. R., Gregory, D. D., Steadman, J. A., Tomkins, A. G., Lounejeva, E., Danyushevsky, L. V., Halpin, J A., Maslennikov, V., Sack, P. J., Mukherjee, I., Berry, R., & Hickman, A. (2015). Gold in the oceans through time. Earth and Planetary Science Letters, 428, 139-150.

Leat, P. T., Livermore, R. A., Millar, I. L., & Pearce, J. A. (2000). Magma supply in back-arc spreading centre segment E2, East Scotia Ridge. Journal of Petrology, 41(6), 845-866.

Lim, D., Kim, H., Kim, J., Jeong, D., &Kim, D. (2020). Mercury proxy for hydrothermal and submarine volcanic activities in the sediment cores of Central Indian Ridge. Marine Pollution Bulletin, 159, 111513.

Little, S. H., Vance, D., McManus, J., Severmann, S., & Lyons, T. W. (2017). Copper isotope signatures in modern marine sediments. Geochimica et Cosmochimica Acta, 212, 253-273.

Livermore, R., Cunningham, A., Vannests, L., & Larter, R. (1997). Subduction influence on magma supply at the East Scotia Ridge. Earth and Planetary Science Letters, 150(3-4), 261-275.

Lyons, W. B., & Fitzgerald, W. F. (1983). Trace metals speciation in nearshore anoxic and suboxic pore waters. In Trace Metals in Sea Water (pp. 621-641). Springer, Boston, MA.

Martin, J. H., Knauer, G. A., & Gordon, R. M. (1983). Silver distributions and fluxes in north-east Pacific waters. Nature, 305(5932), 306-309.

McKay, J. L., & Pederson, T. F., (2008). The accumulation of silver in marine sediments: A link to biogenic Ba and marine productivity. Global Biogeochemical Cycles, 22(4).

Moffett, J. W., & Brand, L. E. (1996). Production of strong, extracellular Cu chelators by marine cyanobacteria in response to Cu stress. Limnology and oceanography, 41(3), 388-395.

Metz, S., & Trefry, J. H. (2000). Chemical and mineralogical influences on concentrations of trace metals in hydrothermal fluids. Geochimica et Cosmochimica Acta, 64(13), 2267-2279.

Morford. J. L., Kalnejais, L. H., Helman, P., Yen, G., & Reinard, M. (2008). Geochemical cycling of silver in marine sediments along an offshore transect. Marine chemistry, 110(1-2), 77-88.

Morse, J. W., & Luther Iii, G. W. (1999). Chemical influences on trace metal-sulfide interactions in anoxic sediments. Geochimica et Cosmochimica Acta, 63(19-20), 3373-3378.

Mills, R. A., & Elderfield, H. (1995). Rare earth element geochemistry of hydrothermal deposits from the active TAG Mound, 26 N Mid-Atlantic Ridge. Geochimica et Cosmochimica Acta, 59(17), 3511-3524.

Mottl, M. J. (1983). Metabasalts, axial hot springs, and the structure of hydrothermal systems at mid-ocean ridges. Geological Society of America Bulletin, 94(2), 161-180.

Nissen, C., Vogt, M., Münnich, M., Gruber, N., & Haumann, F. A. (2018). Factors controlling coccolithophore biogeography in the Southern Ocean. Biogeosciences, 15(22), 6997-7024.

Noble, A. E., Lamborg, C. H., Ohnemus, D. C., Lam, P. J., Goepfert, T. J., Measures, C. I., Frame, C. H., Casciotti, K. L., DiTullio, G. R., Jennings, J., & Saito, M. A. (2012). Basin-scale

inputs of cobalt, iron, and manganese from the Benguela-Angola front to the South Atlantic Ocean. Limnology and oceanography, 57(4), 989-1010.

Passow, U. (1991). Species-specific sedimentation and sinking velocities of diatoms. Marine biology, 108(3), 449-445.

Pearson, R. G. (1963). Hard and soft acids and bases. Journal of the American Chemical society, 85(22), 3533-3539.

Pereira, S. I., Diehl, A., McDermott, J. M., Pape, T., Klose, L., Strauss, H., Bohrmann, G., & Bach, W. (2022). Geochemistry of hydrothermal fluids from the E2-segment of the East Scotia Ridge: Magmatic input, reaction zone processes, fluid mixing regimes and bioenergetic landscapes. Frontiers in Marine Science, 9, 765648.

Pérez, L. F., Hernández-Molina, F. J., Lodolo, E., Bohoyo, F., Galindo-Zaldívar, J., & Maldonado, A. (2019). Oceanographic and climatic consequences of the tectonic evolution of the southern scotia sea basins, Antarctica. Earth-Science Reviews, 198, 102922.

Plass, A., Retschko, A. K., Türk, M., Fischer, T., & Scholz, F. (2022). A novel device for trace metal-clean sampling of bottom water and suspended particles at the ocean's lower boundary: The Benthic Trace Profiler. Limnology and Oceanography: Methods, 20(2), 102-114.

Resing, J. A., Sedwick, P. N., German, C. R., Jenkins, W. J., Moffett, J. W., Sohst, B. M., & Tagliabue, A. (2015). Basin-scale transport of hydrothermal dissolved metals across the South Pacific Ocean. Nature, 523(7559), 200-203.

Reid, W. D., Sweeting, C. J., Wigham, B. D., Zwirglmaier, K., Hawkes, J. A., McGill, R. A., Linse, K., & Polunin, N. V. (2013). Spatial differences in East Scotia Ridge hydrothermal vent food webs: influences of chemistry, microbiology and predation on trophodynamics. PLoS One, 8(6), e65553.

Richter, D. J. (2013). Effects of trace metals on diatom export products from the euphotic zone and significance for biogeochemical cycles. University of California, San Diego.

Rogers, A. D., Tyler, P. A., Connelly, D. P., Copley, J. T., James, R., Larter, R. D., Linse, K., Mills, R. A., Garabato, A. N., Pancost, R. D., Pearce, D. A., Polunin, N. V. C., German, C. R., Shank, T., Boersch-Supan, P. H., Alker, B. J., Aquilina, A. Bennett, S. A., Clarke, A., Dinley, R. J. J., Graham, A. G. C., Green, D. R. H., Hawkes, J, A., Hepburn, L., Hilario, A., Huevenne, V., A. I., Marsh, L., Ramierez-Llodra, E., Reid, W. D. K., Roterman, C. N., Sweeting, C. J., Thatje, S., & Zwirglmaier, K. (2012). The discovery of new deep-sea hydrothermal vent communities in the Southern Ocean and implications for biogeography. PLoS biology, 10(1), e1001234.

Sachs, O., Sauter, E. J., Schlüter, M., van der Loeff, M. M. R., Jerosch, K., & Holby, O. (2009). Benthic organic carbon flux and oxygen penetration reflect different plankton provinces in the Southern Ocean. Deep sea research part I: Oceanographic research papers, 56(8), 1319-1335.

Sander, S. G., & Koschinsky, A. (2011). Metal flux from hydrothermal vents increased by organic complexation. Nature Geoscience, 4(3), 145-150.

Saito, M. A., Moffett, J. W., & DiTullio, G. R. (2004). Cobalt and nickel in the Peru upwelling region: A major flux of labile cobalt utilized as a micronutrient. Global Biogeochemical Cycles, 18(4).

Sawlowicz, Z. (1993). Iridium and other platinum-group elements as geochemical markers in sedimentary environments. Paleogeography, Palaeoclimatology, Palaeoecology, 104(1-4), 253-270.

Schmidt, K., Garbe-Schönberg, D., Koschinsky, A., Strauss, H., Jost, C. L., Klevenz, V., & Königer, P. (2011). Fluid elemental and stable isotope composition of the Nibelungen

hydrothermal field (8 18′ S, Mid-Atlantic Ridge): constraints on fluid–rock interaction in heterogeneous lithosphere. Chemical Geology, 280(1-2), 1-18.

Seeberg-Elverfeldt, J., Schlüter, M., Feseker, T., & Kölling, M. (2005). Rhizon sampling of porewaters near the sediment-water interface of aquatic systems. Limnology and oceanography: Methods, 3(8), 361-371.

Seewald, J. S., & Seyfried Jr, W. E. (1990). The effect of temperature on metal mobility in subseafloor hydrothermal systems: constraints from basalt alteration experiments. Earth and Planetary Science Letters, 101(2-4), 388-403.

Seyfried Jr, W. E., & Ding, K. (1993). The effect of redox on the relative solubilities of copper and iron in Cl-bearing aqueous fluids at elevated temperatures and pressures: an experimental study with application to subseafloor hydrothermal systems. Geochimica et Cosmochimica Acta, 57(9), 1905-1917.

Shaw, T. J., Gieskes, J. M., & Jahnke, R. A. (1990). Early diagenesis in differing depositional environments: the response of transition metals in pore water. Geochimica et Cosmochimica Acta, 54(5), 1233-1246.

Sprenk, D., Weber, M. E., Kuhn, G., Rosén, P., Frank, M., Molina-Kescher, M., Liebetrau, V., & Röhling, H. G. (2013). Southern Ocean bioproductivity during the last glacial cycle–new detection method and decadal-scale insight from the Scotia Sea. Geological Society, London, Special Publications, 381(1), 245-261.

Steiner, Z., Lazar, B., Torfstein, A., & Erez, J. (2017). Testing the utility of geochemical proxies for paleoproductivity in oxic sedimentary marine settings of the Gulf of Aqaba, Red Sea. Chemical Geology, 473, 40-49.

Sunda, W. G. (1989). Trace metal interactions with marine phytoplankton, Biological Oceanography, 6(5-6), 411-442.

Sunda, W. G. (2012). Feedback interactions between trace metal nutrients and phytoplankton in the ocean. Frontiers in microbiology, 3, 204.

Swanner, E. D., Planavsky, N. J., Lalonde, S. V., Robbins, L. J., Bekker, A., Rouxel, O. J., Saito, M. A., Kappler, A., Mojzsis, S. J., & Konhauser, K. O. (2014). Cobalt and marine redox evolution. Earth and Planetary Science Letters, 390, 253-263.

Tivey, M. K. (2007). Generation of seafloor hydrothermal vent fluids and associated mineral deposits. Oceanography, 20(1), 50-65.

Turekian, K. K., & Wedepohl, K. H. (1961). Distribution of the elements in some major units of the earth's crust. Geological society of America bulletin, 72(2), 175-192.

Viollier, E., Jézéquel, D., Michard, G., Pèpe, M., Sarazin, G., & Alberic, P. (1995). Geochernical study of a crater lake (Pavin Lake, France): Trace-element behaviour in the monimolimnion. Chemical Geology, 125(1-2), 61-72.

Wagner, M., Hendy, I. L., & Lai, B. (2022). Characterizing Ag uptake and storage in the marine diatom Thalassiosira pseudonana: Implications for Ag biogeochemical cycling. Marine Chemistry, 104175.

Williams-Jones, A. E., & Heinrich, C. A. (2005). 100th Anniversary special paper: vapor transport of metals and the formation of magmatic-hydrothermal ore deposits. Economic Geology, 100(7), 1287-1312.

Zabel, M., & Schulz, H. D. (Eds.). (2006). Marine geochemistry. Springer.

Zhou, C., Gao, Y., Gaulier, C., Luo, M., Zhang, X., Bratkic, A., Davison, W., & Baeyens, W. (2020). Advances in understanding mobilization processes of trace metals in marine sediments. Environmental Science & Technology, 54(23), 15151-15161.

APPENDICES

Table A1: Solid phase trace metal concentrations.

Core name	Interval depth	Al (wt%)	Mn (ppm)	Fe (ppm)	Co (ppm)	Cu (ppm)	Ag (ppm)
14-1-MUC	1.5	3.31	1624.7	25050.1	9.47	75.69	0.739
	2.5	3.21	1805.1	23333.5	9.10	69.81	0.20
	4	4.86	1844.6	35882.2	12.22	107.1	0.317
	6	2.56	1541.6	19055.3	7.56	56.98	0.201
	8	4.14	2865.0	30623.3	14.28	101.73	0.273
	11	4.24	3086.7	31476.6	12.39	98.54	0.242
	14	4.19	1654.6	30455	11.46	89.97	0.212
	18	5.02	3037.3	36893.3	13.91	100.14	0.243
	22	5.62	2846.0	41104	14.00	94.25	0.261
	27	4.37	1065.6	34013.1	10.55	81.32	0.212
	31	3.48	2768.0	26122.2	10.77	81.76	0.333
15-2-MUC	0.5	3.31	2250.1	24525.4	9.87	74.43	0.249
	1.5	3.52	651.9	28492.6	8.00	83.88	0.229
	2.5	3.30	2780.4	24208.1	10.22	76.59	0.278
	4	3.80	3841.7	27537.2	12.23	89.59	0.292

Table 1A: *(continued).*

Core name	Interval depth	Al (wt%)	Mn (ppm)	Fe (ppm)	Co (ppm)	Cu (ppm)	Ag (ppm)
	6	3.68	3822.9	26701.9	11.82	81.95	0.183
	8	3.21	5228.5	23365.4	11.16	78.71	0.156
	11	3.10	851.6	22630.4	8.85	78.33	0.156
	14	3.91	430.6	26773.8	7.29	80.66	0.188
	18	4.03	472.9	27898.4	7.76	71.12	0.208
	22	4.74	2506.2	34485.4	23.07	94.13	0.203
	27	5.65	1002.2	42016.0	11.32	84.59	0.291
	32	3.94	542.5	28182.6	8.95	92.41	0.191
	37	3.74	1103.5	27093.7	8.51	75.92	0.185
22-2-MUC	0.5	2.95	925.5	19659.7	8.24	57.17	0.198
	1.5	2.75	813.5	18453.8	7.68	51.32	0.196
	2.5	2.91	900.8	19285.9	8.18	55.04	0.173
	4	2.74	1074.3	18439.0	7.58	53.58	0.154
	6	3.04	909.0	19492.6	9.07	53.79	0.171
	8	2.99	1130.7	19524.6	13.61	54.86	0.161
	11	3.07	299.5	21048.4	6.35	55.39	0.152
	14	3.65	330.8	25091.2	7.28	60.11	0.175
	18	3.51	333.1	26380.9	6.92	74.34	0.161
	22	3.84	336.3	34899.0	8.38	66.03	0.291

Table 1A: *(continued).*

Core name	Interval depth	Al (wt%)	Mn (ppm)	Fe (ppm)	Co (ppm)	Cu (ppm)	Ag (ppm)
	27	4.05	367.7	24340.9	7.26	72.98	0.375
	32	3.69	280.8	21774.0	6.55	39.95	0.177
25-2-MUC	0.5	8.11	1394.2	71738.6	25.13	168.81	0.239
	1.5	5.45	3268.1	48235.7	18.92	167.59	0.272
	2.5	5.98	3534.6	52072.3	20.61	186.35	0.270
	4	8.76	1661.0	80484.1	31.58	148.28	0.202
	6	5.32	2503.1	45571.7	17.28	161.71	0.195
	8	5.18	1494.7	43690.5	14.61	147.34	0.212
	11	5.50	1023.8	47734.6	13.86	142.87	0.225
	14	6.61	2747.5	58283.9	21.55	151.76	0.218
	18	6.74	4018.9	59616.8	20.17	144.3	0.238
	20	7.57	4621.5	66882.6	21.48	135.68	0.236
37-2-MUC	0.0	6.34	10483.9	54379.1	20.05	155.47	0.234
	0.5	6.40	8966.6	53983.7	19.57	15.97	0.230
	1.5	6.58	9599.0	56219.9	20.18	161.44	0.212
	2.5	6.34	9340.8	54539.1	19.72	155.61	0.222
	4	6.34	10483.8	54379.1	20.05	155.47	0.200
	6	7.12	14100	63320.4	23.34	160.62	0.342
	8	7.66	973.4	60022.1	19.83	186.41	0.251
	11	7.01	1162.2	57502.5	20.29	189.51	0.251
	14	4.90	3043.7	44774.1	17.41	157.68	0.200

Table 1A: *(continued).*

Core name	Interval depth	Al (wt%)	Mn (ppm)	Fe (ppm)	Co (ppm)	Cu (ppm)	Ag (ppm)
48-1-MUC	18	7.51	1419.1	68202.5	25.66	167.08	0.210
	22	8.25	1476.6	71077.6	28.60	143.37	0.213
	27	4.86	2737.4	42820.7	17.16	150.91	0.200
	0.5	6.46	1016.9	33289.8	10.58	59.27	0.293
	1.5	6.43	1050.9	32364.0	10.29	56.64	0.273
	2.5	5.81	926.7	28578.6	9.02	51.12	0.247
	4	7.55	982.0	34921.0	10.53	55.04	0.320
	6	7.93	958.8	38949.1	12.91	53.78	0.325
	8	8.56	938.3	37647.7	10.42	51.79	0.392
	11	8.51	1023.6	50281.6	19.69	81.30	0.250
	14	6.39	793.6	40287.1	15.76	67.16	0.188

Table A2: Trace metal concentrations within the porewater.

Core name	Interval depth	Mn (µM)	Fe (µM)	Co (nM)	Cu (nM)	Ag (nM)
14-1	0	0.00	0.20	1.83	10.28	0.08
	0.5	0.00	0.10	2.11	102.73	1.30
	1.5	0.00	0.00	2.52	105.57	1.43
	2.5	0.00	0.10	2.55	113.31	1.69
	4	0.00	0.30	2.69	128.95	2.19
	6	0.00	0.00	2.52	127.77	4.15
	8	1.40	0.10	2.89	125.07	0.81
	11	9.80	0.00	2.53	107.74	0.78
	14	11.40	0.00	3.18	78.33	0.83
	18	17.30	0.00	3.59	79.29	0.44
	22	22.30	0.00	3.61	94.21	0.69
	27	27.00	0.00	6.41	76.83	0.40
	31	28.60	0.10	7.72	77.64	0.35
15-2	0	0.00	0.00	1.98	6.95	0.10
	0.5	0.00	0.00	2.62	118.66	0.67
	1.5	1.40	0.00	2.38	92.65	4.15
	2.5	0.00	0.00	2.98	102.30	6.56
	4	0.00	0.00	2.32	123.24	5.63
	6	0.00	0.00	1.94	74.86	6.29
	8	0.00	0.00	2.31	84.08	1.48

Table 2A: *(continued).*

Core name	Interval depth	Mn (µM)	Fe (µM)	Co (nM)	Cu (nM)	Ag (nM)
	11	0.00	0.00	3.45	81.26	0.38
	14	2.20	N/A	N/A	N/A	N/A
	18	10.5	0.00	18.62	126.46	1.02
	22	24.7	0.00	31.21	85.21	0.78
	27	33.4	0.00	63.72	92.44	0.67
	32	50.0	0.00	92.42	91.81	0.42
	37	39.9	0.00	88.44	81.21	0.37
22-2	0	0.01	0.89	1.83	5.74	0.09
	0.5	0.00	0.00	3.01	245.46	1.27
	1.5	0.00	0.00	1.87	104.51	1.80
	2.5	0.02	0.00	1.78	94.29	1.53
	3.5	0.00	0.00	1.74	106.91	1.29
	6	0.00	0.04	1.87	100.40	0.67
	8	0.05	0.00	2.05	99.44	0.62
	11	0.21	0.00	2.43	81.05	0.30
	14	1.93	0.00	7.31	80.47	0.45
	18	3.43	0.00	16.98	85.17	0.42
	22	4.88	6.35	20.73	43.38	0.25
	27	6.16	23.37	30.97	17.58	0.20
	32	7.00	39.63	30.33	18.63	0.13

Table 2A: *(continued).*

Core name	Interval depth	Mn (µM)	Fe (µM)	Co (nM)	Cu (nM)	Ag (nM)
25-2	0	0.04	0.00	1.65	0.00	0.13
	0.5	0.08	0.04	1.77	163.42	2.58
	1.5	0.10	0.02	1.98	103.67	3.20
	2.5	0.07	0.11	2.63	107.34	5.67
	4	0.12	0.12	2.89	65.22	1.99
	6	0.18	0.12	2.73	119.69	1.77
	8	0.11	0.35	2.55	77.42	2.08
	11	0.62	0.39	1.74	142.78	0.47
	14	0.02	0.11	1.58	59.44	0.36
	18	0.15	0.11	1.71	43.50	0.32
	20	0.24	0.22	1.22	45.69	0.27
37-2	0	0.00	0.04	1.31	4.16	0.02
	0.5	0.03	0.00	2.11	127.66	1.00
	1.5	0.01	0.00	2.49	69.19	1.85
	2.5	0.01	0.00	1.68	69.29	1.53
	4	0.03	0.00	1.65	83.42	0.96
	6	0.02	0.00	1.79	59.48	0.90
	8	8.10	1.17	14.10	141.17	0.15
	11	39.33	11.69	38.44	73.07	0.10
	14	107.23	19.81	81.48	30.34	0.05

Table 2A *(continued).*

Core name	Interval depth	Mn (µM)	Fe (µM)	Co (nM)	Cu (nM)	Ag (nM)
	18	135.23	21.43	93.25	39.39	0.28
	22	186.44	13.83	128.50	76.33	0.32
	27	229.10	12.70	117.47	106.01	0.28
48-1	0	0.00	0.00	1.74	9.52	0.21
	0.5	0.03	0.12	2.68	255.82	0.64
	1.5	0.02	0.00	1.81	121.20	1.03
	2.5	0.01	0.20	1.89	123.95	0.79
	4	0.03	0.00	2.07	108.76	0.37
	6	0.00	0.00	2.94	38.01	0.52
	8	0.01	0.00	2.37	38.78	0.28
	11	0.62	0.20	130.65	15.78	0.50
	14	1.65	4.53	64.31	20.33	0.10
	16	3.14	2.10	45.49	19.38	0.25

VITA

Calli Madison Provenza

Candidate for the Degree of

Master of Science

Thesis: DEPOSITIONAL BEHAVIORS OF TRACE METALS AROUND HYDROTHERMAL VENTS IN THE SCOTIA

Major Field: Geology

Biographical:

Education:

Completed the requirements for the Master of Science in geology at Oklahoma State University, Stillwater, Oklahoma in December, 2022.

Completed the requirements for the Bachelor of Science in geology at Texas A&M University, College Station, TX/United States of America in 2019.

Experience:

Exploration Geology Intern | SSR Mining
MAY 2022 – AUGUST 2022

Undergraduate Researcher over the Petrology of The Trans-Mexican Volcanic Belt | Texas A&M University
JANUARY 2018 – MAY 2019

Professional Memberships:

Geological Society of America (SEG)
American Geophysical Union (AGU)
American Association of Petroleum Geologists (AAPG)